(12)

DNA 5991F

EARLY TIME STARFISH CALCULATIONS

F. E. Fajen
R. W. Kilb

Mission Research Corporation
735 State Street
Santa Barbara, California 93101

1 February 1982

Final Report for Period 30 April 1979—15 June 1980

CONTRACT No. DNA 001-79-C-0276

THIS WORK WAS SPONSORED BY THE DEFENSE NUCLEAR AGENCY
UNDER RDT&E RMSS CODE B322079464 S99QAXHC06243 H2590D.

Prepared for
Director
DEFENSE NUCLEAR AGENCY
Washington, DC 20305

UNCLASSIFIED

SECURITY CLASSIFICATION OF THIS PAGE (When Data Entered)

REPORT DOCUMENTATION PAGE	READ INSTRUCTIONS BEFORE COMPLETING FORM
1 REPORT NUMBER: DNA 5991F	2 GOVT ACCESSION NO.: AD-A131 179	3 RECIPIENT'S CATALOG NUMBER:
4 TITLE (and Subtitle): EARLY TIME STARFISH CALCULATIONS	5 TYPE OF REPORT & PERIOD COVERED: Final Report for Period 30 Apr 79 to 15 Jun 80
	6 PERFORMING ORG. REPORT NUMBER: MRC-R-572
7 AUTHOR(s): F. E. Fajen, R. W. Kilb	8 CONTRACT OR GRANT NUMBER(s): DNA 001-79-C-0276
9 PERFORMING ORGANIZATION NAME AND ADDRESS: Mission Research Corporation, 735 State Street, Santa Barbara, CA 93101	10 PROGRAM ELEMENT, PROJECT, TASK AREA & WORK UNIT NUMBERS: Subtask S99QAXHC062-43
11 CONTROLLING OFFICE NAME AND ADDRESS: Director, Defense Nuclear Agency, Washington, D.C. 20305	12 REPORT DATE: 1 February 1982
	13 NUMBER OF PAGES: 80
14 MONITORING AGENCY NAME & ADDRESS (if different from Controlling Office)	15 SECURITY CLASS (of this report): UNCLASSIFIED
	15a DECLASSIFICATION DOWNGRADING SCHEDULE: N/A since UNCLASSIFIED

16 DISTRIBUTION STATEMENT (of this Report)

Approved for public release; distribution unlimited.

17 DISTRIBUTION STATEMENT (of the abstract entered in Block 20, if different from Report)

18 SUPPLEMENTARY NOTES

This work was sponsored by the Defense Nuclear Agency under RDT&E RMSS Code B322079464 S99QAXHC06243 H2590D.

19 KEY WORDS (Continue on reverse side if necessary and identify by block number)

Nuclear Burst above 150 km.
Expansion from 0 to 1 sec.
Blast Wave Behavior
Collisionless Magnetohydrodynamics
Debris Energy Patches
Conjugate Patches
Velocity Spectrum of Conjugate Patches

20 ABSTRACT (Continue on reverse side if necessary and identify by block number)

In this report, we present results from recent CMHD (Collisionless Magnetohydrodynamics) code calculations of the early time (0 to 1 sec.) evolution of the Starfish event. The emphasis of this report is on the velocity spectrum of the energy going to the conjugate patches. We present a parameter study, utilizing results from eight simplified, "CMHD-like" calculations, which demonstrates the dominant role played by ionizing collisions during the blast wave expansion.

DD FORM 1 JAN 73 1473 EDITION OF 1 NOV 65 IS OBSOLETE

UNCLASSIFIED

SECURITY CLASSIFICATION OF THIS PAGE (When Data Entered)

TABLE OF CONTENTS

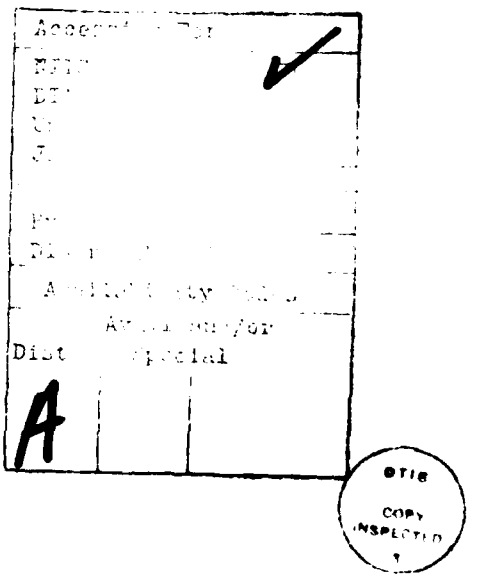

LIST OF ILLUSTRATIONS

LIST OF ILLUSTRATIONS (Continued)

LIST OF ILLUSTRATIONS (Continued)

LIST OF ILLUSTRATIONS (Concluded)

SECTION I
INTRODUCTION

For nuclear bursts occurring above about 150 km altitude and below about 600 km, an important aspect of the burst phenomenology is the debris energy patch. Analysis of photographic data taken following the Starfish nuclear test has indicated that one-fourth to one-half of the kinetic yield of the weapon arrived in each magnetic conjugate region during the first few seconds after the burst.

The existence of the debris energy patch was predicted prior to the Starfish event by Longmire, et. al.,[1] and their prediction proved to be essentially correct. The current understanding of the phenomenon is that weapon debris ions and air ions that are accelerated to high velocities (10^7 cm/sec to a few times 10^8 cm/sec) by the expanding debris-air blast wave, stream parallel to the (distorted) geomagnetic field lines from the burst region to each magnetic conjugate, where they are stopped by ordinary atomic collisions and thereby deliver their energy to the background air, heating and ionizing it. Ionization thus produced in the debris energy patches may persist for several hours after the burst. It is likely to develop structure - i.e., striations - and it therefore is expected to degrade the performance of communication links which propagate through it.

Under DNA funding, a highly specialized computer code was developed at Mission Research Corporation (MRC) to treat the early time phenomenology of nuclear bursts in the 150 km to 600 km altitude range. This code, known as CMHD (Collisionless Magnetohydrodynamics), briefly

described in Section 2 of this report, is fully described and documented in References 2 and 3.

Seven high altitude burst calculations, covering a range of burst altitudes and yields, have been completed with CMHD, and have been published in reference 3. The first of these was a simulation of Starfish. Comparisons of predicted northern conjugate region (NCR) power as a function of time after burst were made with the published power-time curve inferred from the photographic data, and adequate agreement was obtained.

However, the Starfish photographic data do not yield sufficient information to verify all aspects of the CMHD code. And, unfortunately, the KLYSMA - SCORPIO - CYLWHAT family of codes at the Naval Research Laboratory (NRL), when applied to Starfish, have given results which differ in certain respects from those of CMHD. In particular, the two sets of results differ with regard to the velocity spectrum of the fast ions which stream from the burst area to the conjugate regions to generate the debris energy patches. The NRL spectrum tends to be harder, to cause the patch ionization to occur at lower altitudes, where molecular deionization can proceed rapidly, and thus produce less persistent ionization than does the CMHD spectrum (if the energy/cm^2 of the deposition along the field lines is less than $\sim 10^7$ ergs/cm^2 so that molecular species still predominate after the NRL-type energy deposition).

This report presents results of two additional Starfish runs that have been made with the CMHD code as part of the continuing effort to resolve this disagreement between MRC and NRL with regard to the debris energy patch spectrum. These additional CMHD calculations are described in Section 3.

In Section 4, several simplified "CMHD-like" calculations are presented, which demonstrate the degree to which the debris energy patch spectrum is sensitive to different aspects of the physics in the CMHD code. The result of this study is that the spectrum is highly sensitive to the rate at which background air is ionized by collisional processes in the expanding blast wave. The detailed treatment given to these collisional processes in the CMHD code, and the lack of a corresponding treatment in the NRL codes is believed to be the primary source of the discrepancy between the MRC and NRL results.

SECTION 2
THE CMHD CODE

The physics embodied in the CMHD code, the derivation of the mathematical equations, and the code itself are documented in references 2 and 3. The CMHD code is believed (at MRC) to represent the current state of the art for early time nuclear burst phenomenology in the relevant altitude regime. A very brief synopsis of the CMHD physics now follows.

Ideally, one would like to solve the Boltzmann transport equation for each ion and neutral species, resulting in several distribution functions, each a function of time and six space and velocity variables. However, this is well beyond the capacity of present day computers, and we are forced to eliminate some of the independent variables. One space variable and two velocity variables can be eliminated by assuming azimuthal symmetry - appropriate for the case of an initially vertical geomagnetic field - and by assuming that all ions in the same spatial location have the same average velocity in the direction perpendicular to $\vec{B}$. The latter assumption is justified on the basis of momentum coupling in the transverse-to-$\vec{B}$ direction, which is generally believed to occur on a length scale of an ion gyro radius or shorter. Appropriate moments of the Boltzmann equation are used, then, to derive a set of equations which are fluid-like in the transverse-to-$\vec{B}$ direction, but which retain the arbitrary distribution function in parallel velocity space. That is, ions move together as a fluid in the perpendicular direction, but are allowed to stream independently in the parallel direction.

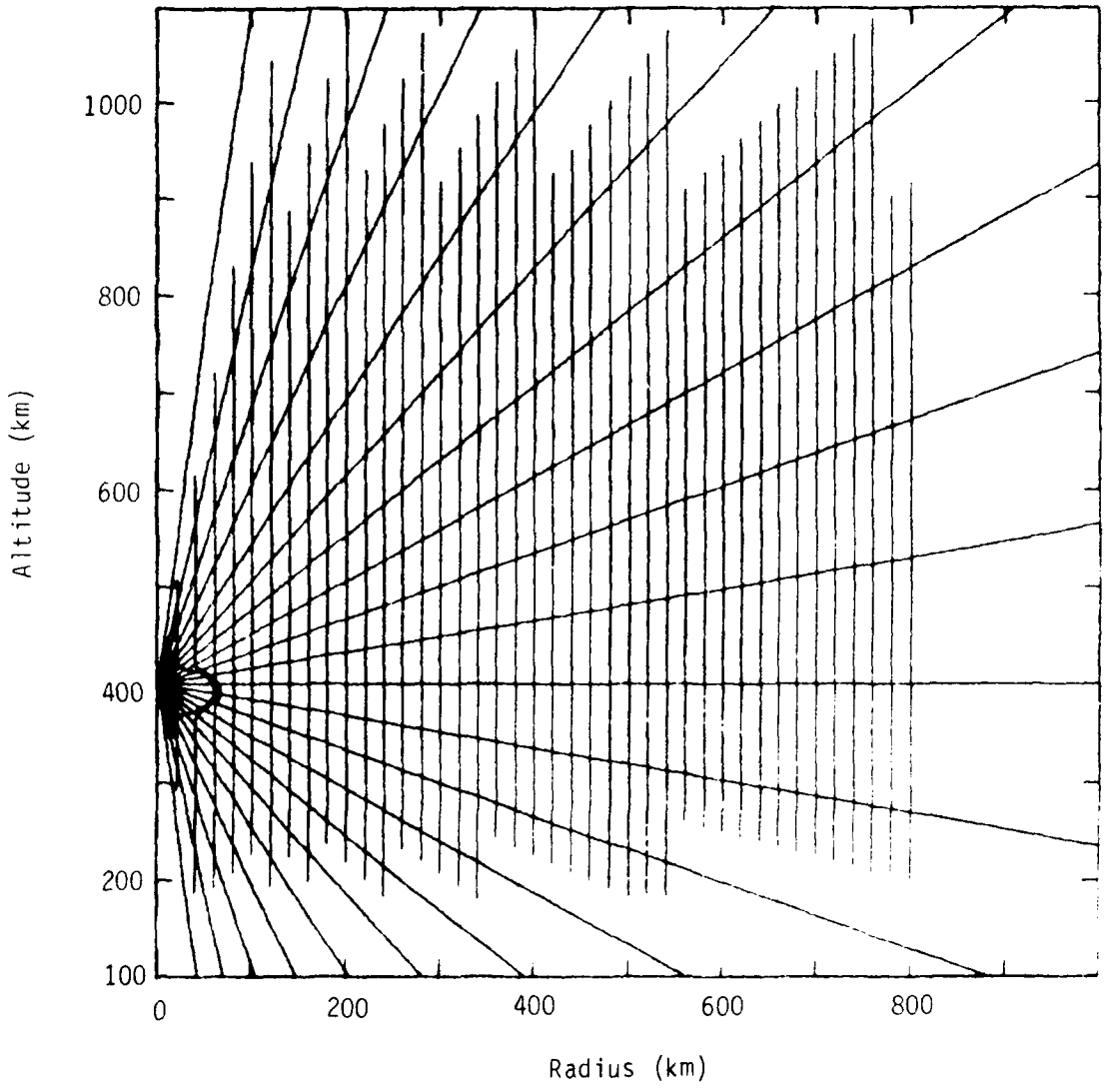

Figure 1. The CMHD computational grid used for Starfish. Radial lines emanating from the burst point are Eulerian surfaces, while the vertical lines which represent magnetic flux surfaces, are Lagrangian.

The CMHD computational grid, illustrated in Figure 1, consists of cells, enclosed by two sets of surfaces. The radial surfaces emanating from the burst point remain fixed in space (Eulerian surfaces) as the ions move upward or downward through them from one cell into a neighboring one. The other set of surfaces, initially vertical, represent magnetic flux surfaces, and move outward with the ions (Lagrangian surfaces) as they expand away from the immediate vicinity of the burst. Initially, each cell contains ions present in the ambient ionosphere plus ions created by X-rays from the burst. Further ionization may be generated by deposition of UV energy and by collisional ionization by ions or electrons of background neutrals. This collisional ionization of neutrals is an important source of ions, which can cause an exponential increase in the ion mass within a flux tube as the blast wave expansion progresses.

Figures 2 and 3 show the configuration of the CMHD grid at several times during the blast wave expansion for one of our recent Starfish simulations. At .025 seconds, the problem initialization time, only the two innermost flux surfaces are distorted. As the expansion proceeds, the volume of the magnetic bubble increases dramatically, and by 0.4 seconds, all of the flux surfaces are distorted, some quite severely. Simulations such as the one depicted here are usually run out to a problem time of one to two seconds after burst time.

As a cell is compressed and set in motion, the ions within that cell acquire "transverse thermal" energy as they are picked up by the moving field lines and gyrate about these field lines. There may also be plasma turbulent processes which excite transverse thermal modes, but such processes are not treated in detail by CMHD. Rather, the code solves the fluid-like equation derived from the appropriate moment of the Boltzmann equation to obtain the ion transverse thermal energy. If the resulting transverse pressure is sufficiently large compared to the parallel pressure, then the plasma is unstable, and one or more plasma instabilities

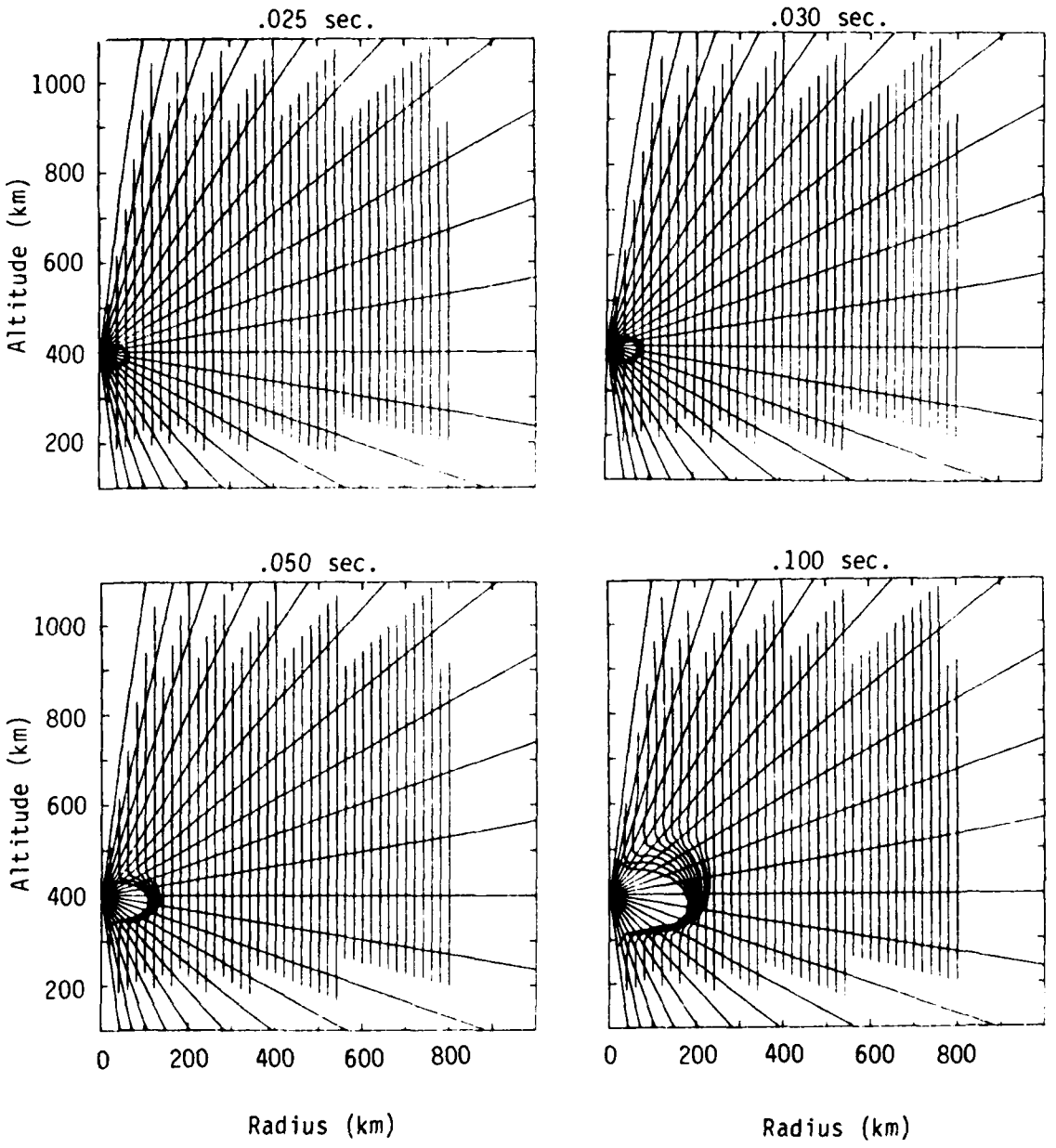

Figure 2. The CMHD computational grid at .025 sec., .03 sec., .05 sec., and .10 sec., during a simulation of the Starfish event.

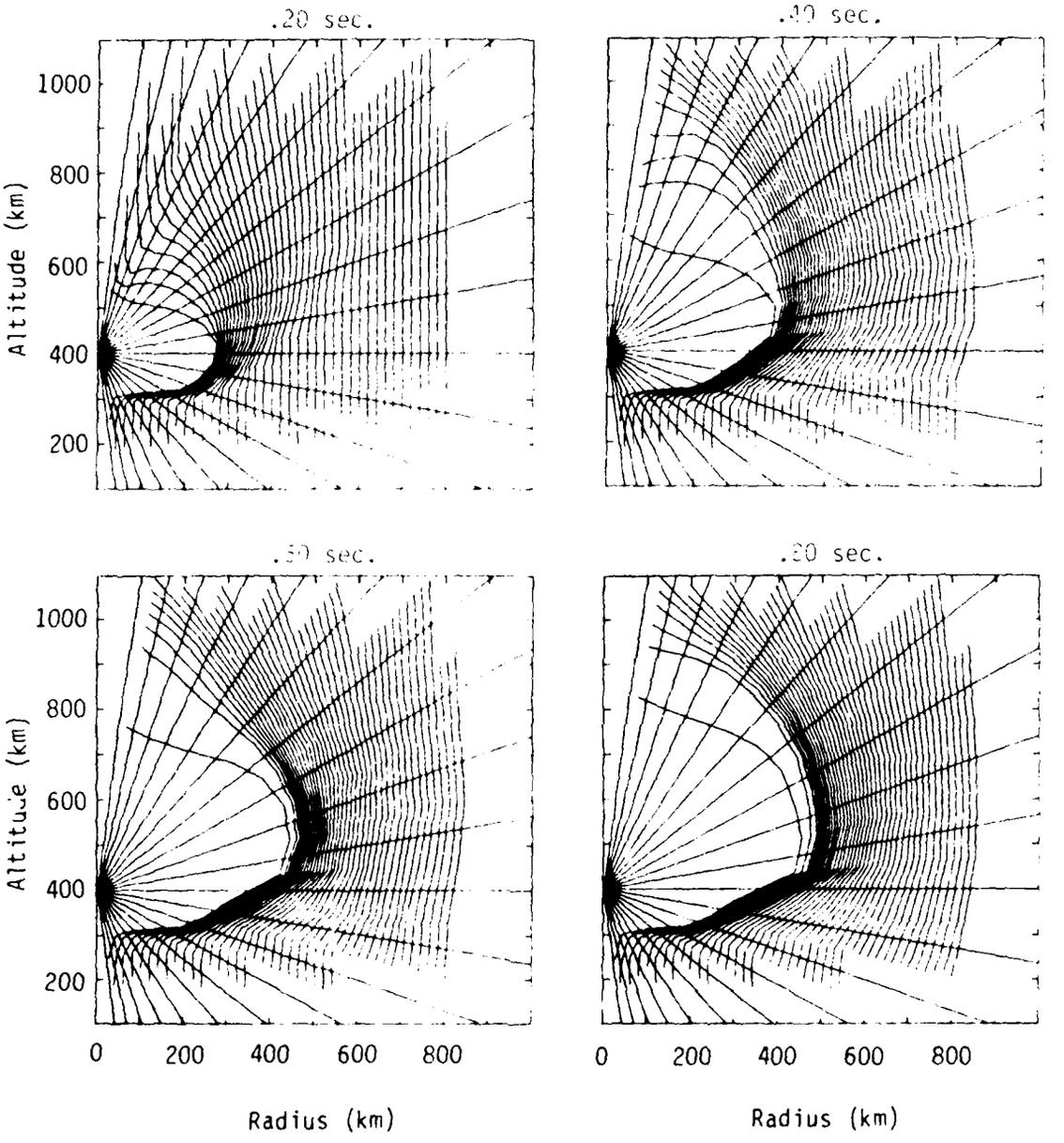

Figure 3. The CMHD computational grid at .20 sec., .40 sec., .60 sec., and .80 sec., during a simulation of the Starfish event.

will turn on, deflecting ion thermal velocities from the transverse direction into the parallel direction. The turn-on condition for the mirror instability[4] is

$$P_\perp - P_\parallel > \frac{P_\parallel}{P_\perp} \frac{B^2}{8\pi} .$$

In the previously published CMHD calculation, this instability was simulated by the SCATTER subroutine, by performing velocity space diffusion to increase $P_\parallel$ at the expense of $P_\perp$ whenever the above condition was met. The result of this was to drive the velocity distribution toward a Maxwellian, which is generally what we would expect from turbulent processes. Other forms of the SCATTER subroutine, simulating other types of scattering in velocity space, have been exercised in recent CMHD calculations, as will be described in Sections 3 and 4.

As the ions follow their independent parallel-to-$\vec{B}$ trajectories, they undergo several interactions. Ions with different parallel velocities interact via ordinary coulomb collisions. This is generally important only at relatively large ion densities such as when the bottom of the grid is below 200 km altitude, and ions created at higher altitudes find themselves streaming through essentially stationary ions created by X-rays and UV. Ions interact with the magnetic field, via the mirror force, which accelerates them from regions of high field strength toward regions of low B, consituting an interchange between transverse thermal energy and parallel streaming energy. As ions stream through a region of curved field lines which is in motion, there is interchange between transverse streaming energy and parallel streaming energy (sling effect). Charge exchange between a moving ion and a stationary neutral can occur, resulting in a stationary ion (which is then swept outward along with the moving magnetic flux surface) and a fast neutral. The resulting fast (or "hot") neutrals are then treated with transport equations similar in complexity

to the ion equations. The neutrals may become collisionally re-ionized, or they may stream out of the computational grid as neutrals. The neutrals which exit the grid in the downward direction constitute an important source of deposition energy in the patch region below the burst. The fast neutrals which exit upward from the grid have more than sufficient energy to escape into interplanetary space, thereby reducing the effective kinetic yield of the burst.

Electrons are heated through coulomb collisions with ions, and also by plasma turbulent processes, to temperatures that would approach several keV, if there were not competing processes which cool them. These cooling processes are (i) ionization of background neutrals, mentioned above as an important source of ion mass, (ii) further ionization of air ions, which can result in significant populations of multiply ionized states of oxygen and nitrogen, and (iii) electronic excitation of these air ions, followed by radiation of ultraviolet (UV) photons. At altitudes below 300 km, the UV radiation is a significant mechanism for cooling the blast wave, as well as for producing ionization in regions outside the current position of the blast wave.

To summarize, then, the CMHD code was designed and developed to compute, for high altitude bursts:

(i) blast wave expansion,

(ii) transport of energy away from the blast wave by fast ions streaming parallel to $\vec{B}$, and the various interactions between these streaming ions and the blast wave,

(iii) charge exchange losses, and subsequent transport and reionization of the resulting fast neutrals, and

(iv) multiple ionization state chemistry, the associated production of UV radiation, and the subsequent deposition of this UV energy.

These processes are highly intertwined and interdependent. Experience has shown that it is necessary to treat them in a self-consistent manner in order to obtain a reliable computation of the energy transport and of the spatial location of final energy deposition for a high altitude nuclear burst, which is the objective of the CMHD code.

SECTION 3
RECENT CMHD CALCULATIONS OF STARFISH

The first full-scale nuclear burst simulation completed with the CMHD code was the Starfish calculation reported in reference 3. This calculation, in common with the other six burst simulations that were presented in the same technical report, gave a velocity spectrum for the debris energy patch which had the approximate* functional form

$$\frac{dE}{dU_{\parallel}} \sim U_{\parallel}^{-1} ,$$

where $\frac{dE}{dU_{\parallel}}$ is the energy per unit velocity delivered to the patch by ions with parallel velocity between $U_{\parallel}$ and $U_{\parallel} + dU_{\parallel}$. This general form is consistent with the time dependence of the observed Starfish total NCR power,[5] which is plotted in Figure 4. Also plotted in Figure 4 is a curve representing the function $f(t) = t^{-1}$. It is seen that the two curves agree quite well, for times after the peak in the power-time curve. Assuming that the time of arrival of the fast ions in the patch region is inversely proportional to the velocity, we have

$$t \sim U^{-1}, \tag{3-1}$$

and thus

$$\frac{dt}{dU} \sim U^{-2}, \tag{3-2}$$

---

* In reference 3, the patch spectrum is fit with a much more elaborate function, which takes into account the spatial dependence of the spectrum. The present discussion is primarily qualitative, so the more approximate functional form used here is quite adequate.

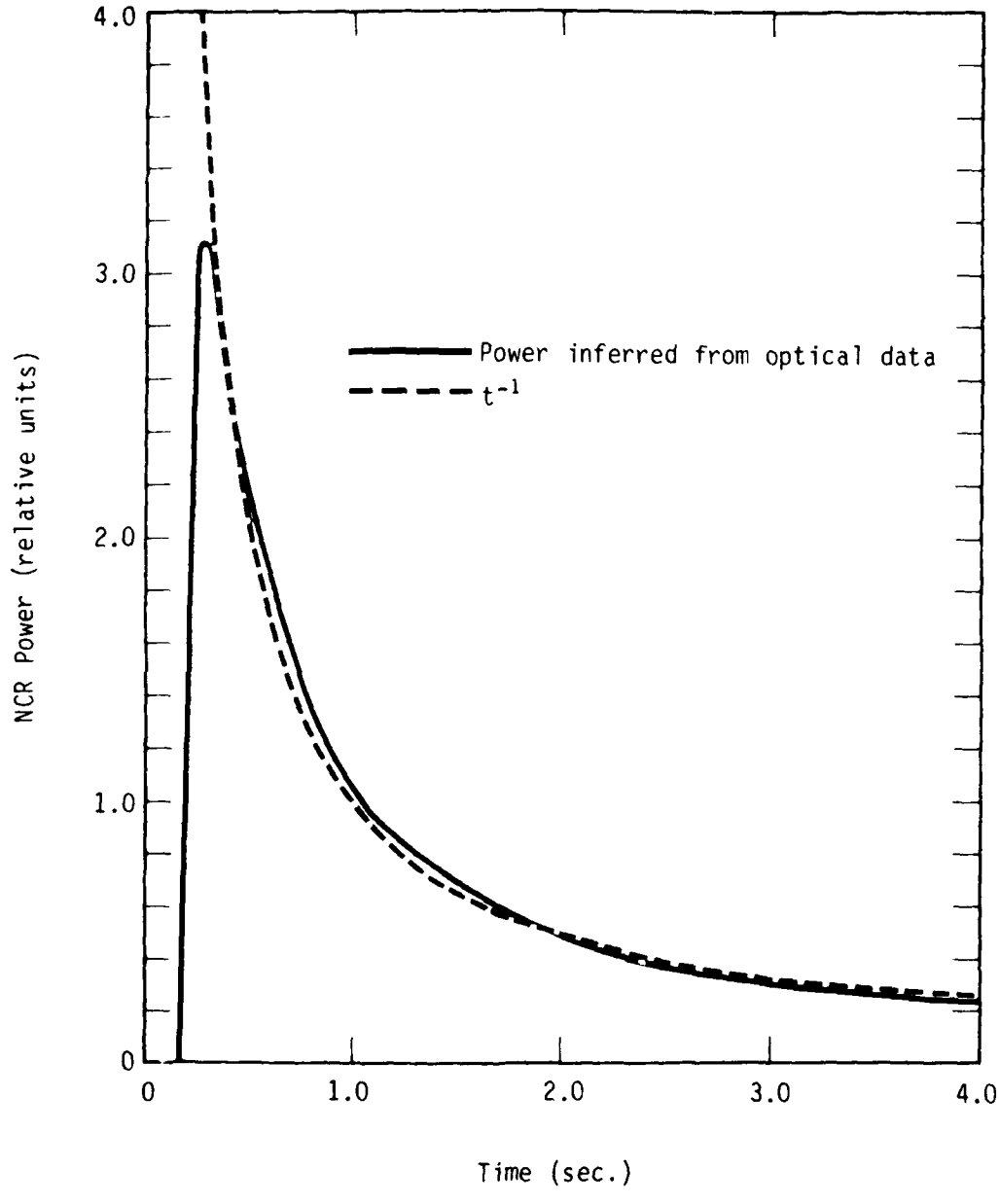

Figure 4. Comparison of Starfish NCR power, as inferred from optical data, with $f(t) = t^{-1}$.

which can be combined with the observed time dependence of the NCR power,

$$\frac{dE}{dt} \sim t^{-1}, \tag{3-3}$$

to yield an estimate of the form of the velocity spectrum, as follows:

$$\frac{dE}{dU} = \frac{dE}{dt} \cdot \frac{dt}{dU} \sim t^{-1} \cdot U^{-2}, \tag{3-4}$$

or,

$$\frac{dE}{dU} \sim (U^{-1})^{-1} \cdot U^{-2} = U^{-1}. \tag{3-5}$$

Thus, it is seen that the Starfish data are consistent with a spatially integrated spectrum which is approximately the same as that predicted by CMHD. Although the exact computed spectral shape is a slowly varying function of spatial location, the general form of equation 3-5 is approximately applicable at all radii.

The NRL results, on the other hand, show considerable dependence on cross-field radius. At small radii, the NRL computed spectrum is more like $\frac{dE}{dU} \sim U^{+1}$. On a spatially integrated basis, however, their results have also been shown to be approximately consistent with the optical data. Kilb[3] compared the NRL and MRC results with each other and with data in considerable detail, and concluded that in spite of the fact that the velocity spectra predictions by the two groups are quite different, and even though the data seem to imply that the form of equation 3-5 is approximately correct, one could not make an iron-clad distinction between the different results on the basis of the published optical power data, which is spatially integrated over the NCR region.

It has therefore been necessary to attempt to resolve the issue on theoretical grounds, which has proved to be a difficult task. As part of this on-going effort to resolve these discrepancies between the NRL and

MRC code results, we have made two additional CMHD runs for the Starfish event. We shall refer to the original calculation as "run A," and to the more recent calculations as "run B" and "run C." Run A used a form of the SCATTER subroutine which performed velocity space diffusion to drive the local velocity distribution toward isotropization whenever the conditions for the mirror instability were met. Dr. Robert Clark, Dr. Peter Palmadesso, and other NRL scientists objected strenuously to this procedure. The NRL philosophy concerning the scattering of energy from transverse thermal modes into parallel stream modes is expressed by the following quotation:[6]

> "We focus our attention on the coupling region for the present. As we have said it contains a highly compressed magnetic field and a mixture of hot air and debris. The debris ions have streaming energies predominantly perpendicular to the field. Coupling instabilities in this medium convert this energy into random transverse motion, heating the debris and air ions anisotropically in the transverse direction so that $T_\perp / T_\parallel \sim 3$. In this way a large part of the transverse streaming energy of the debris ions is transferred quickly to the parallel direction and shared with the ambient ions.
>
> This process results in a peculiar velocity distribution, deficient in specific high velocity values at which ions are streaming out of the coupling region faster than they can be replaced. This distribution, containing, a 'hole' in velocity, is known to suffer an electrostatic instability, the Post-Rosenbluth 'loss cone instability.' The electrostatic fields which are associated with this instability preferentially pitch

angle scatter ions with high transverse velocities ($v_\perp > v_{thermal}$) into the parallel direction, where they stream out the loss cone. The net result of all of the above is the establishment of a quasi-steady state of equilibrium consisting of a continuous flow, out of the loss cone parallel to the magnetic field, of debris and air ions with velocities significantly larger than the transverse thermal, $V_\parallel = \lambda V_{TH\perp}$, $\lambda \sim 2.-2.5$. Thus these escaping ions have a beam-like character."

At a working group meeting at MRC in September, 1979, Palmadesso and Dr. Joseph Workman of Berkeley Research Associates suggested a method of modelling the effects of the Post-Rosenbluth instability in our SCATTER subroutine. They suggested that energy be removed from transverse thermal at the rate

$$\frac{d}{dt} e_\perp = \begin{cases} -(e_\perp - \bar{e}) \dfrac{V_{th}}{L} & \text{if } e_\perp > \bar{e}, \\ 0, \text{ if } e_\perp \leq \bar{e} . \end{cases} \qquad (3\text{-}6)$$

where $e_\perp$ is the transverse thermal energy density at a particular location in the blast wave, $\bar{e}$ is a mean thermal energy chosen so that the system will approach pressure isotropization, V_{th} is the local mean ion thermal speed, and L is a scattering length, proportional to the Debye length. As this energy is removed from transverse thermal, it appears as parallel streaming energy, in the form of air ions traveling at parallel velocities $\pm \lambda V_{th}$, with $\lambda = 2.5$. This procedure became known as the "Workman - Palmadesso formula," and was encoded into our SCATTER subroutine for run B and run C. The effects of these different models for the scattering process are explored in detail in Section 4.

The other change which has been made in CMHD, and which was implemented for run C, was prompted by informal discussions with Dr. Palmadesso of NRL and Dr. Steve Brecht of SAI. As a result of these discussions, we discovered that we had made an unfortunate choice of numerical differencing methods for an equation representing the "sling effect," mentioned in Section 2. During the blast wave expansion there is interchange between energy associated with the expansion transverse to $\vec{B}$ (transverse streaming energy) and energy of ions streaming parallel to $\vec{B}$. The relevant differential equations are

$$\frac{d}{dt} U_{\parallel} = U_{\parallel} V_{\perp} \vec{b} \cdot \nabla \vec{b} \cdot \vec{e}, \tag{3-7}$$

and

$$\frac{d}{dt} V_{\perp} = -U_{\parallel}^2 \vec{b} \cdot \nabla \vec{b} \cdot \vec{e}, \tag{3-8}$$

where $U_{\parallel}$ is the parallel ion velocity, $V_{\perp}$ is the transverse velocity of of the plasma (and the magnetic field lines) and $\vec{b}$ and $\vec{e}$ are unit vectors parallel and transverse to $\vec{B}$, respectively. When ions streaming parallel to $\vec{B}$ find themselves on moving, curved field lines, they will undergo an interchange of energy between parallel and transverse modes, according to these equations. This is simply an expression of the fact that, under these conditions, the unit vectors $\vec{b}$ and $\vec{e}$ are changing in space and in time. Total energy is conserved, of course. The particular numerical method that was chosen for simulating this effect had the unfortunate property of decreasing the parallel energy too much, under certain circumstances. After this discovery, we altered the code to correct the deficiency, and again repeated the Starfish calculation. To summarize, then, there have been three CMHD Starfish calculations: the original one, completed in 1978, and referred to as run A, which utilized the diffusive form of the SCATTER subroutine; run B, completed in 1979, which used the Workman - Palmadesso (WP) form of the SCATTER routine; and run C, which included the WP SCATTER routine and had the problem with the "sling effect" fixed. The three calculations used identical initial and boundary conditions.

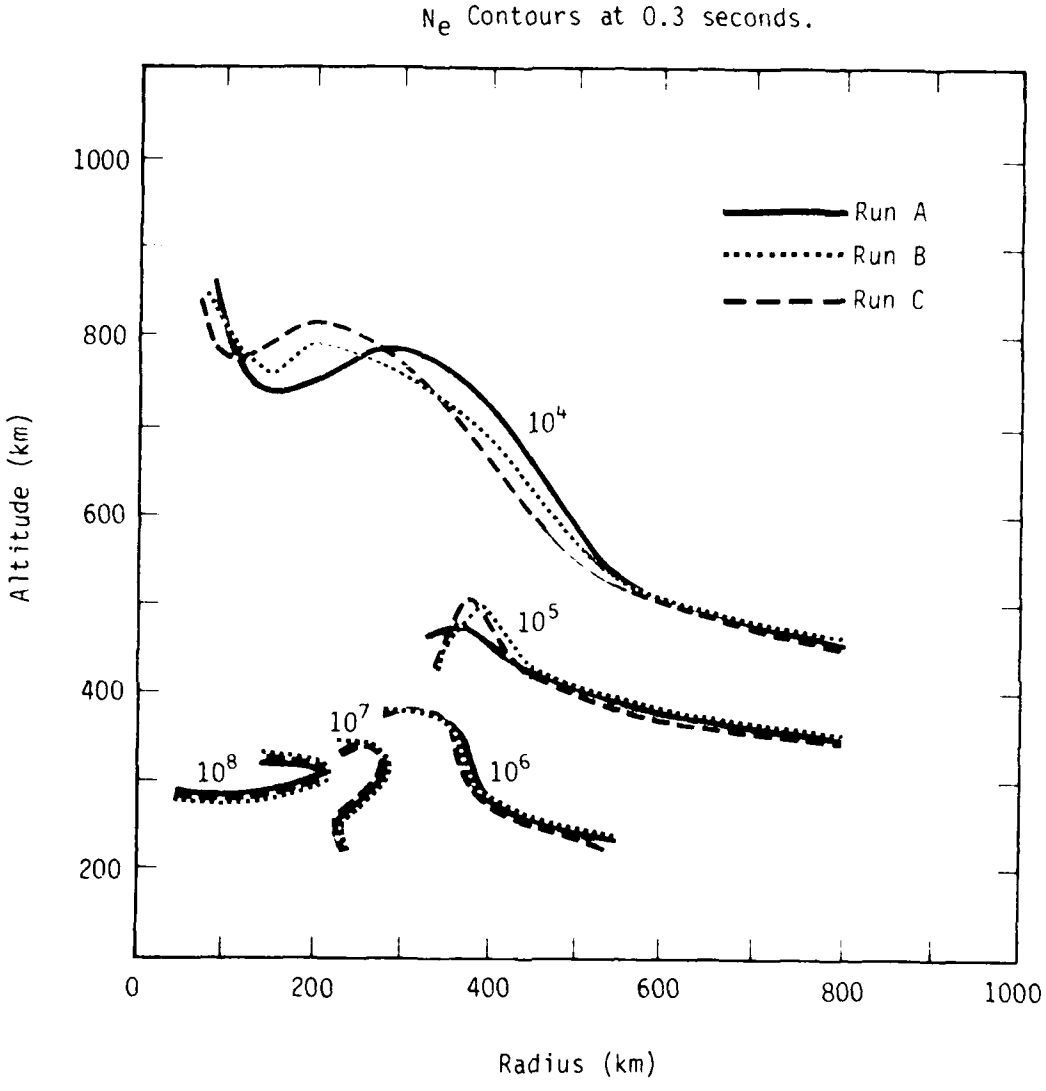

Figure 5. Comparison of N_e contours from the three Starfish simulations. The values contoured are in units of electrons/cm^3. The contour lines terminate at the surface of the burst-produced magnetic bubble and at the edge of the computational grid.

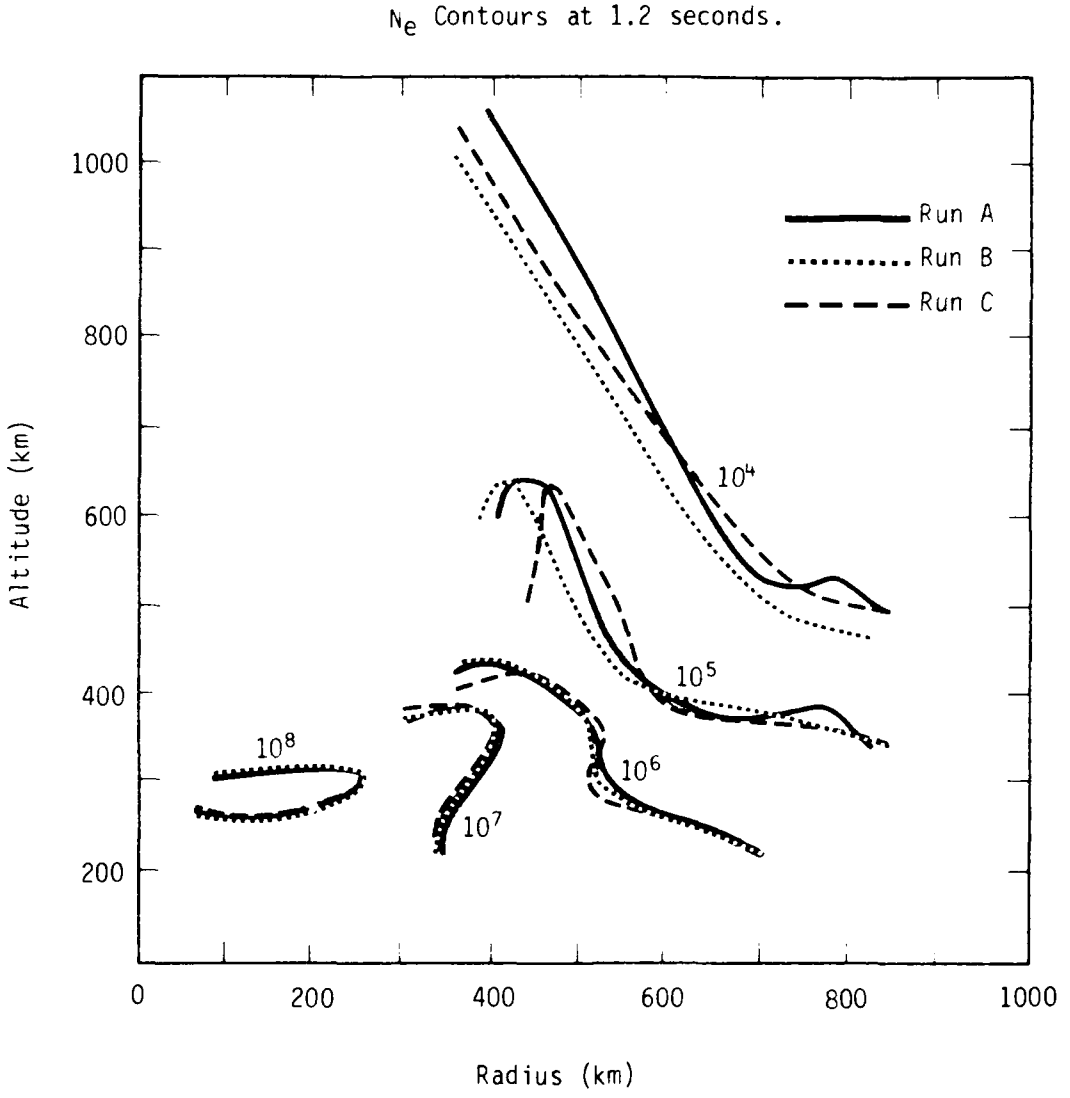

Figure 6. Comparison of N_e contours from the three Starfish simulations. The values contoured are in units of electrons/cm^3. The contour lines terminate at the surface of the burst-produced magnetic bubble and at the edge of the computational grid.

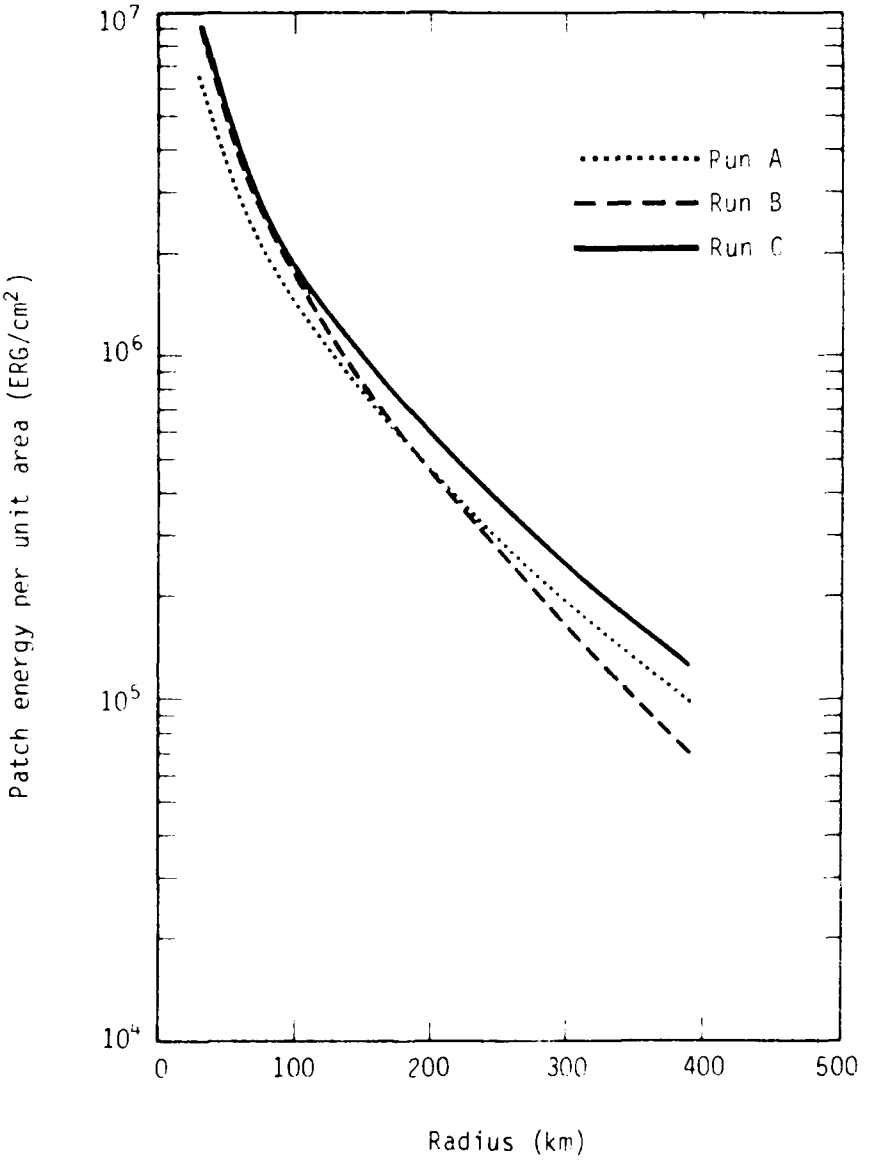

Figure 7. Energy delivered to the downward (NCR) debris energy patch as a function of cross-field radius.

The overall dynamics of the blast wave expansion were affected very little by these changes in the code. Figure 5 and 6 show comparisons of electron density contours at 0.3 seconds and at 1.2 seconds after burst time. These contour plots reveal slight differences in the blast wave expansions. These differences are almost imperceptable in the downward-going section of the blast wave, which is the most important from the standpoint of production of long-lasting ionization. The differences in blast wave expansion are more obvious in the horizontal and above-horizontal directions, but are well within the range of uncertainty which we would assign to any one of the calculations.

The motivation for performing the additional CMHD calculations was to determine the extent to which the debris patch predictions would differ from that of the original Starfish simulation. Figure 7 shows the time-integrated energy flux predictions for the downward patch as a function of cross-field radius. Although the differences are well within the overall range of uncertainty, and should not be viewed as significant, it is worth noting that the three calculations differ in ways that are consistent with the changes that were made in the code. Runs B and C both result in higher time-integrated fluxes at small radii than does the original run. This is a result of using the WP SCATTER subroutine, which deflects more energy into high parallel velocities during the early stages of the blast wave expansion, when the radius of the blast wave is small. The curve from run B then falls below that for run A at larger radii. We might expect this to happen, simply because if more energy is transported away from the blast wave at earlier times, there is less available at later times (and larger radii). The fact that curve C is higher than the others at all radii is a consequence of the changes in implementation of equations 3-7 and 3-8, which resulted in keeping more energy in parallel modes as the ions moved down the distorted geomagnetic field lines.

Of particular interest is the comparison of predictions of patch spectra. Figures 8 through 10 show velocity spectra of energy predicted to arrive in the downward patch within 100 km of the burst field line. Energy reaching the patch in the form of fast ions is plotted in Figure 8, fast neutral energy is shown in Figure 9, and the sum of both ion and neutral energy is given in Figure 10.

The two more recent calculations show an increase in the amount of energy reaching the patch at high velocities. Run C, especially, predicts substantially more energy at velocities above 2000 km/sec. In retrospect, we suspect that the changes made for run C may have overcorrected the earlier deficiencies, and therefore may have actually caused a bigger boost at the high velocity end of the spectrum than is warranted. The qualitative result that runs B and C predict a somewhat harder spectrum than does run A, is to be expected, in view of the changes that were made in the CMHD code. The low velocity end of the spectrum, however, is essentially the same for all three runs. This is an important result, for two reasons. First, it demonstrates that the exact form of the SCATTER subroutine has little impact on this portion of the spectrum, which is comforting in view of the fact that plasma turbulence is essentially impossible to model in detail. Also, since the slower ions deposit their energy at higher altitudes, where the resulting ionization will tend to persist longer, the low velocity portion of the patch spectrum is more important from the military systems viewpoint.

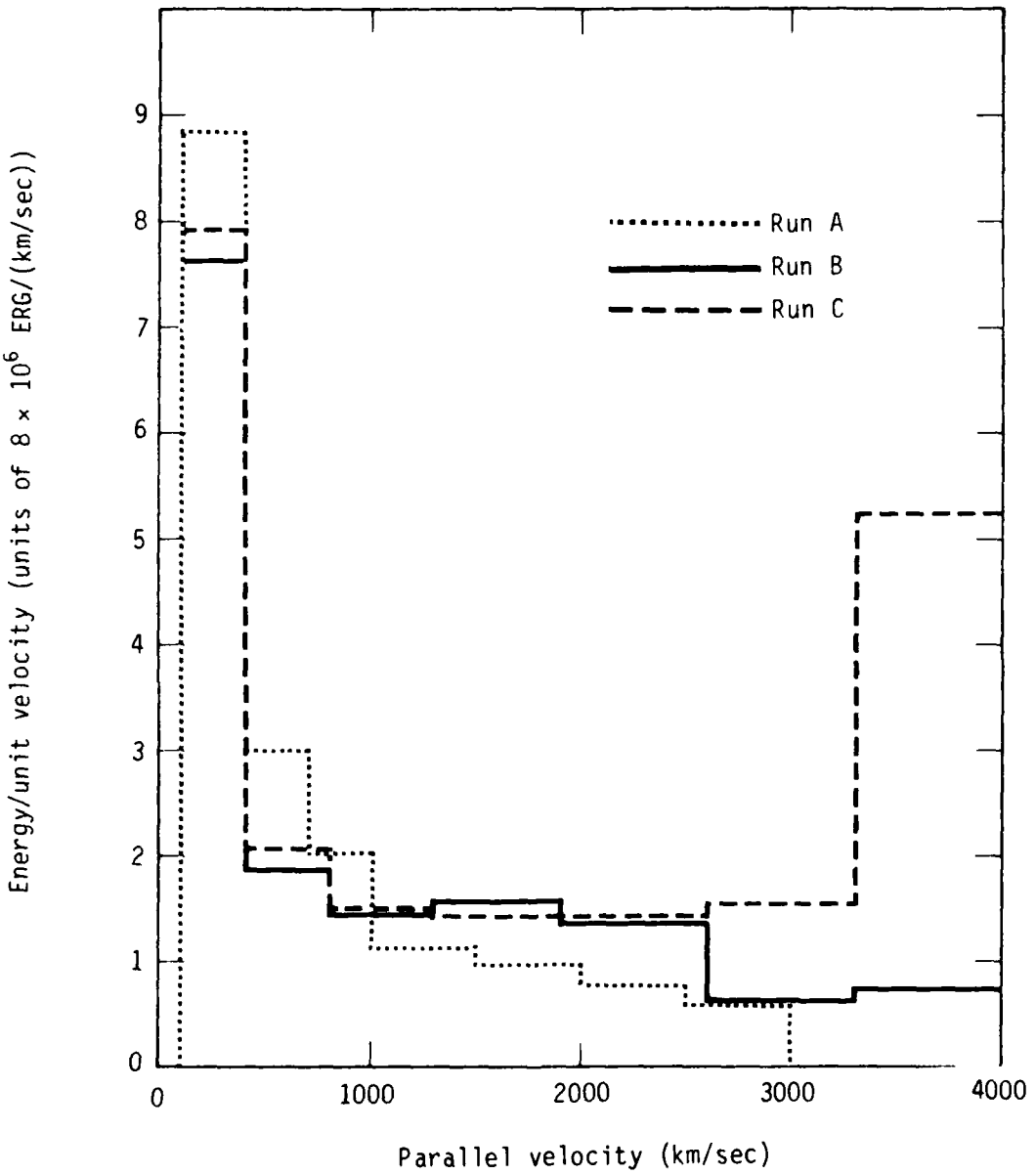

Figure 8. Comparison of fast ion contribution to downward (NCR) debris energy patch spectra.

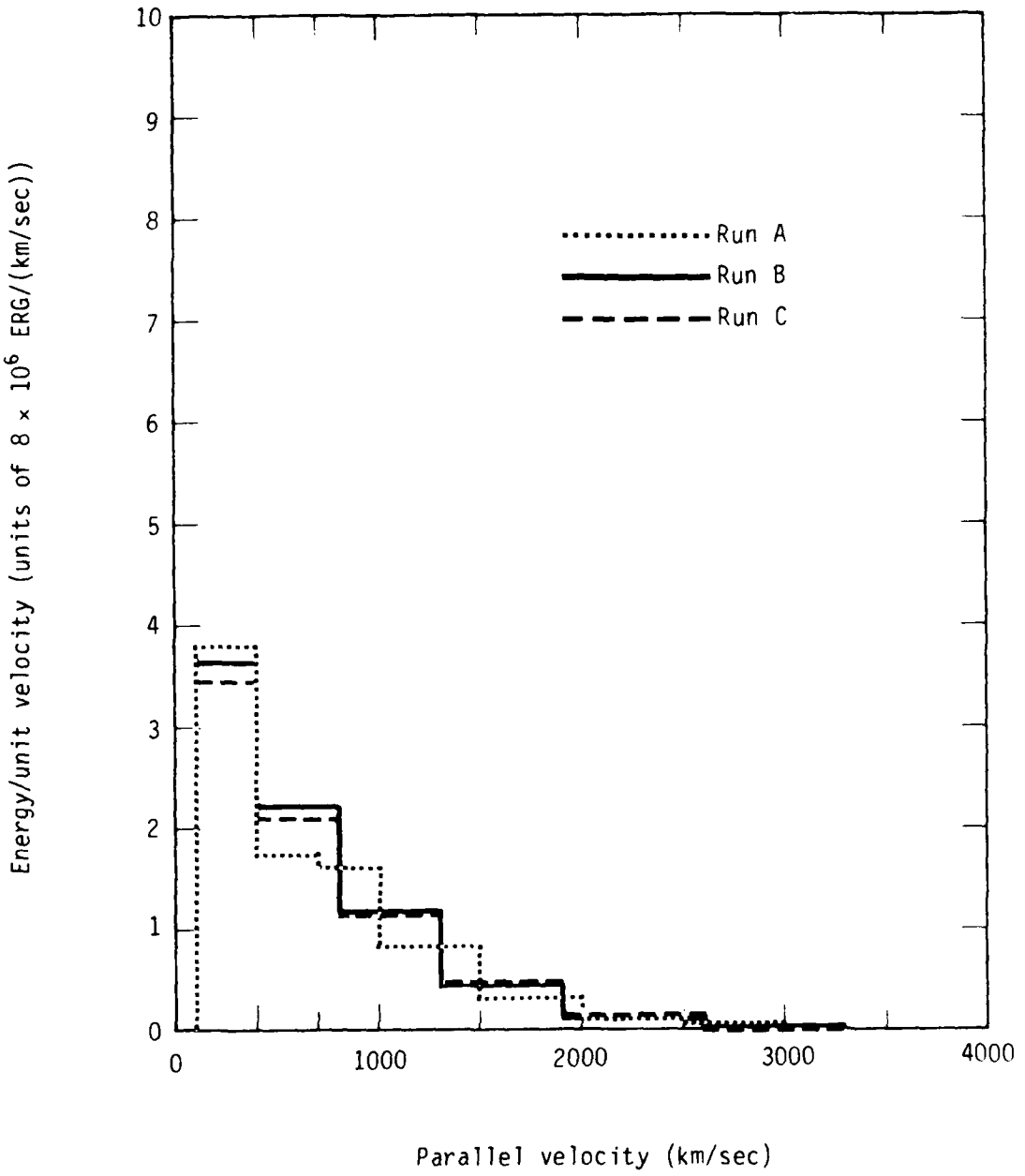

Figure 9. Comparison of fast neutral contribution to downward (NCR) debris energy patch spectra.

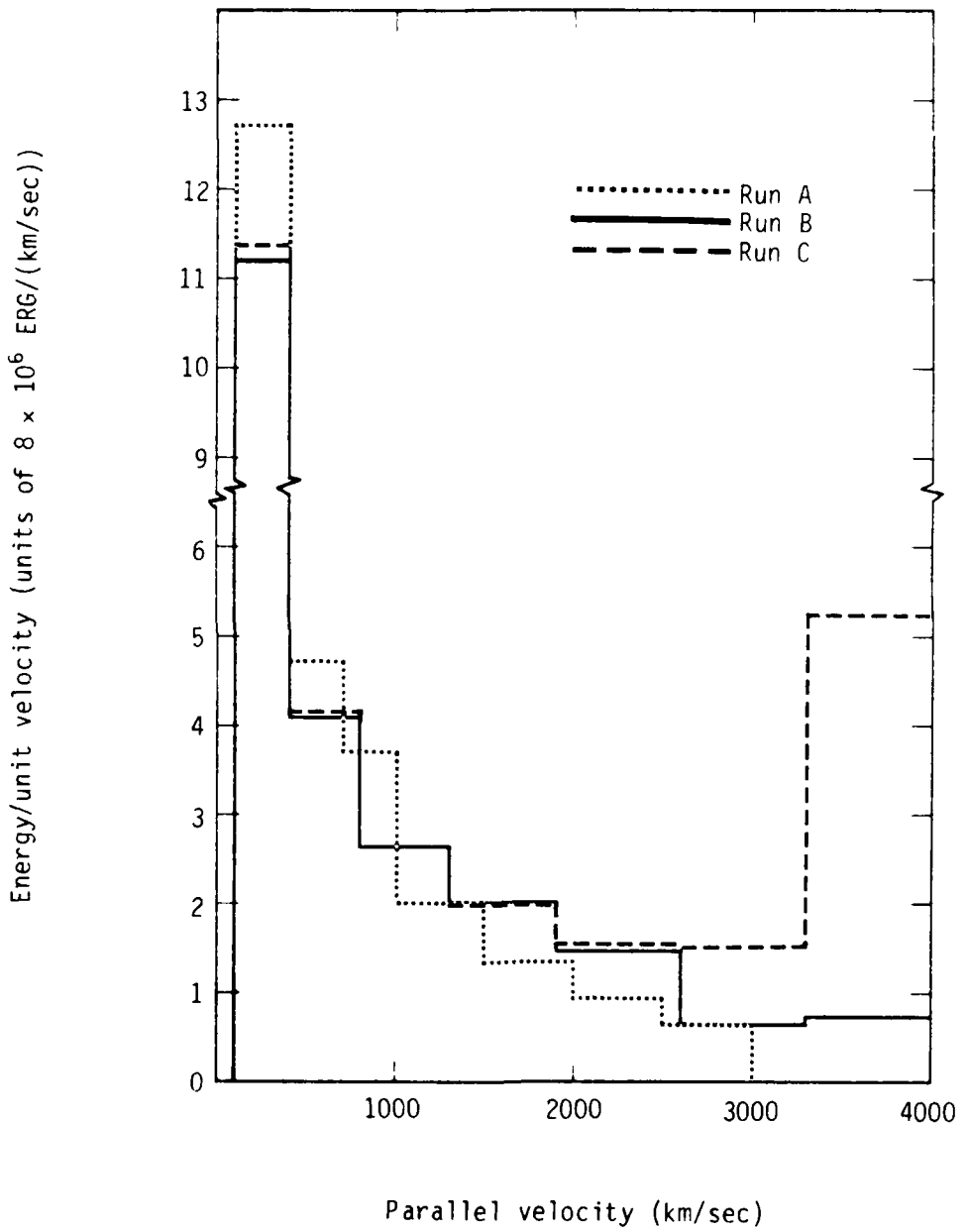

Figure 10. Comparison of downward (NCR) debris energy patch spectra.

SECTION 4
PATCH SPECTRUM SENSITIVITY STUDY

To obtain more detailed information about the sensitivity of the debris energy patch spectrum to certain features of the physics embodied in CMHD, we performed a series of simplified calculations for a single magnetic flux tube. We chose flux tube number five from the most recent Starfish simulation, which was initially vertical and included the volume between cylindrical radii of 80 km and 100 km. The flux tube geometry and the sources of energy and mass were taken from the full CMHD calculations.

The geometry of this flux tube is shown in Figure 11 at four different times during the blast wave expansion. At .05 seconds after burst time, the flux tube has been compressed and distorted in the horizontal sector and in two or three sectors above and below horizontal. At later times, more of the flux tube is involved in the expansion, and by .80 seconds, the distortion away from the ambient configuration is quite extreme, involving all of the flux tube between about 250 km altitude and 1000 km altitude. As the blast wave compresses the flux tube, ions and electrons are given transverse thermal energy, resulting in large transverse temperatures. Collisional processes then ionize more of the background air, increasing the ion mass within the flux tube. The rate at which transverse thermal energy and ion mass were added to this flux tube were determined for each angular sector from the output of the full CMHD calculation. These rates, integrated over all sectors, are shown in Figure 12. The time integrals of these rates are plotted in Figure 13.

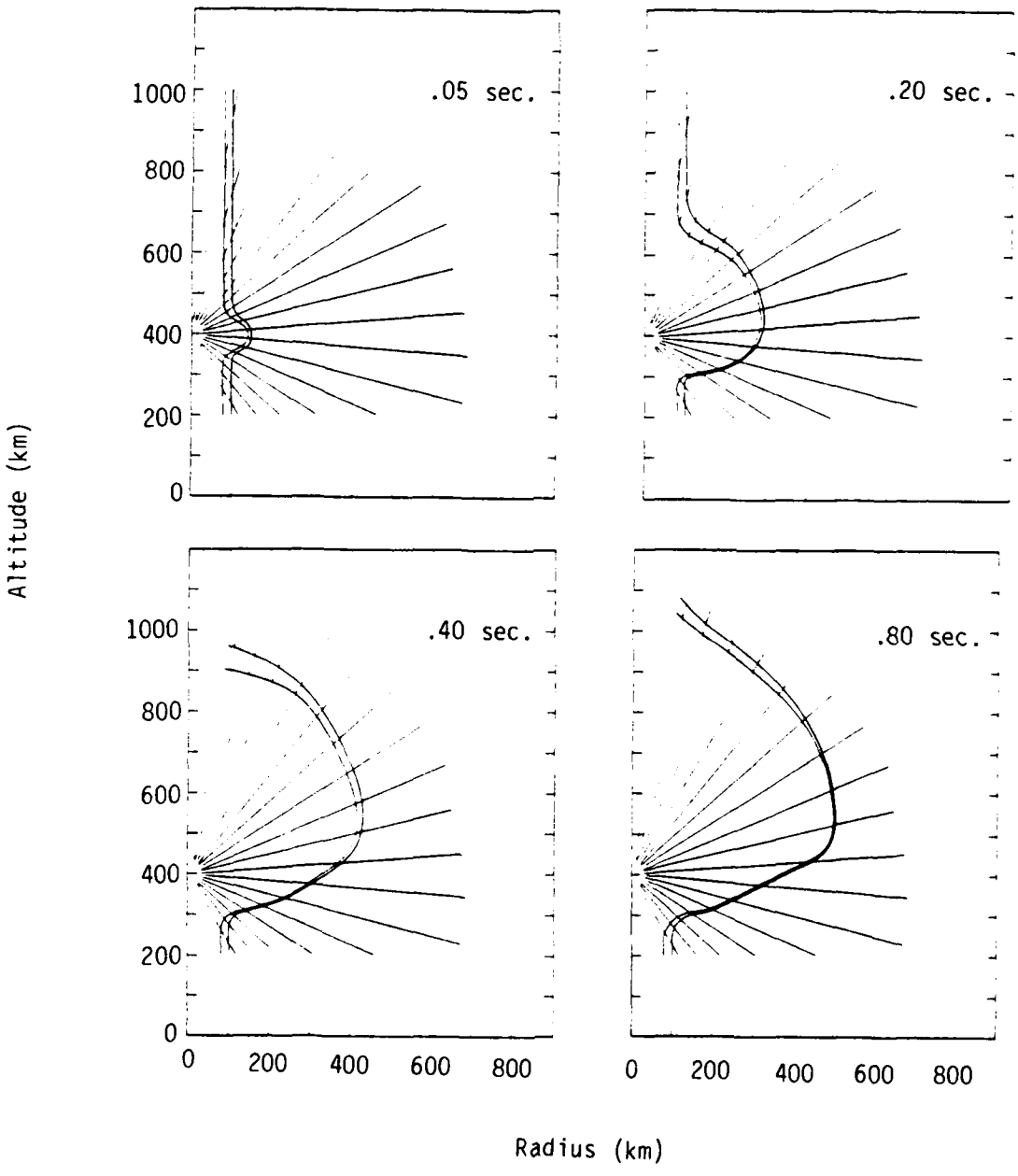

Figure 11. Geometry of flux tube no. 5 at various times during the blast wave evolution.

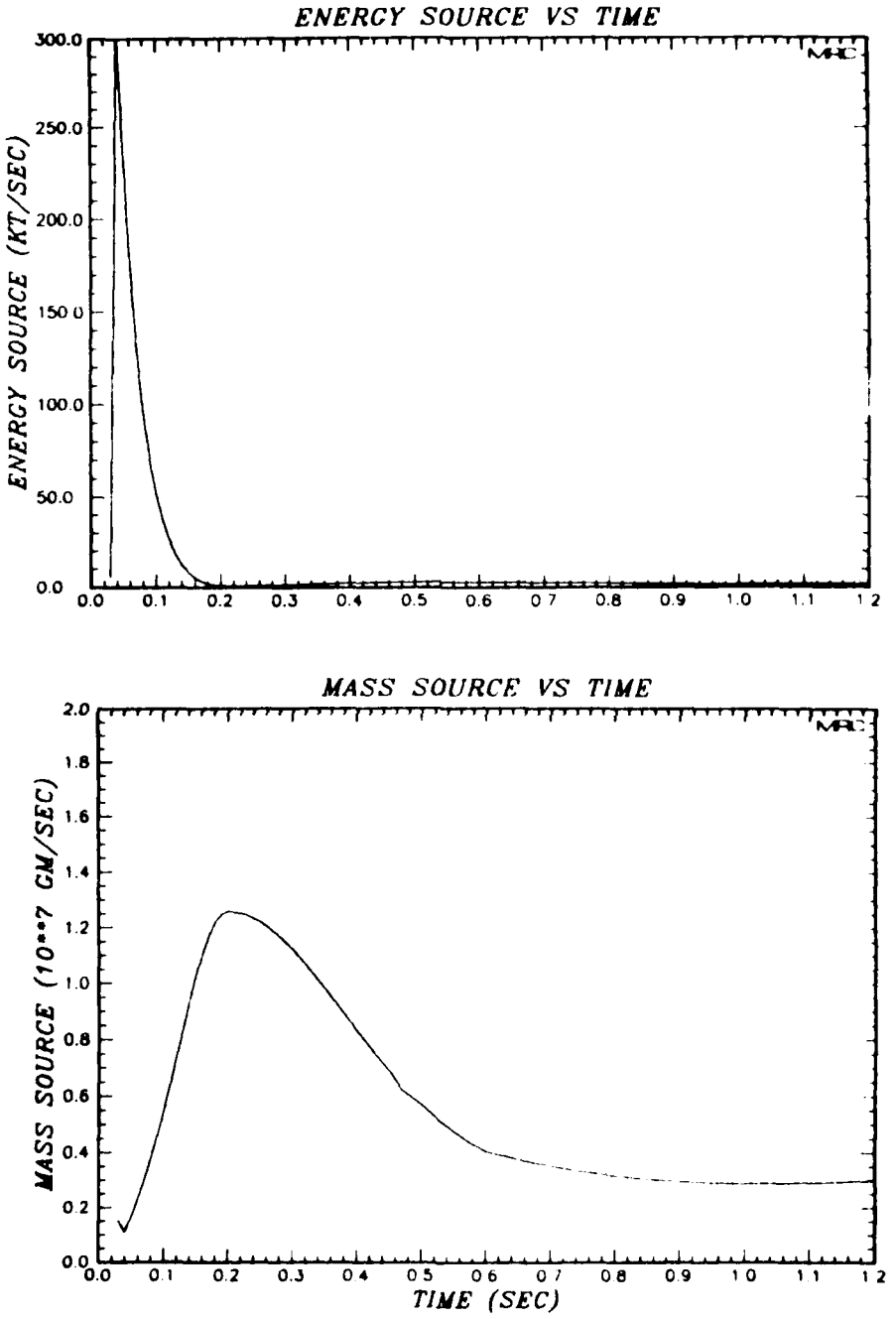

Figure 12. Energy and mass sources for the entire flux tube, as determined from the full CMHD run.

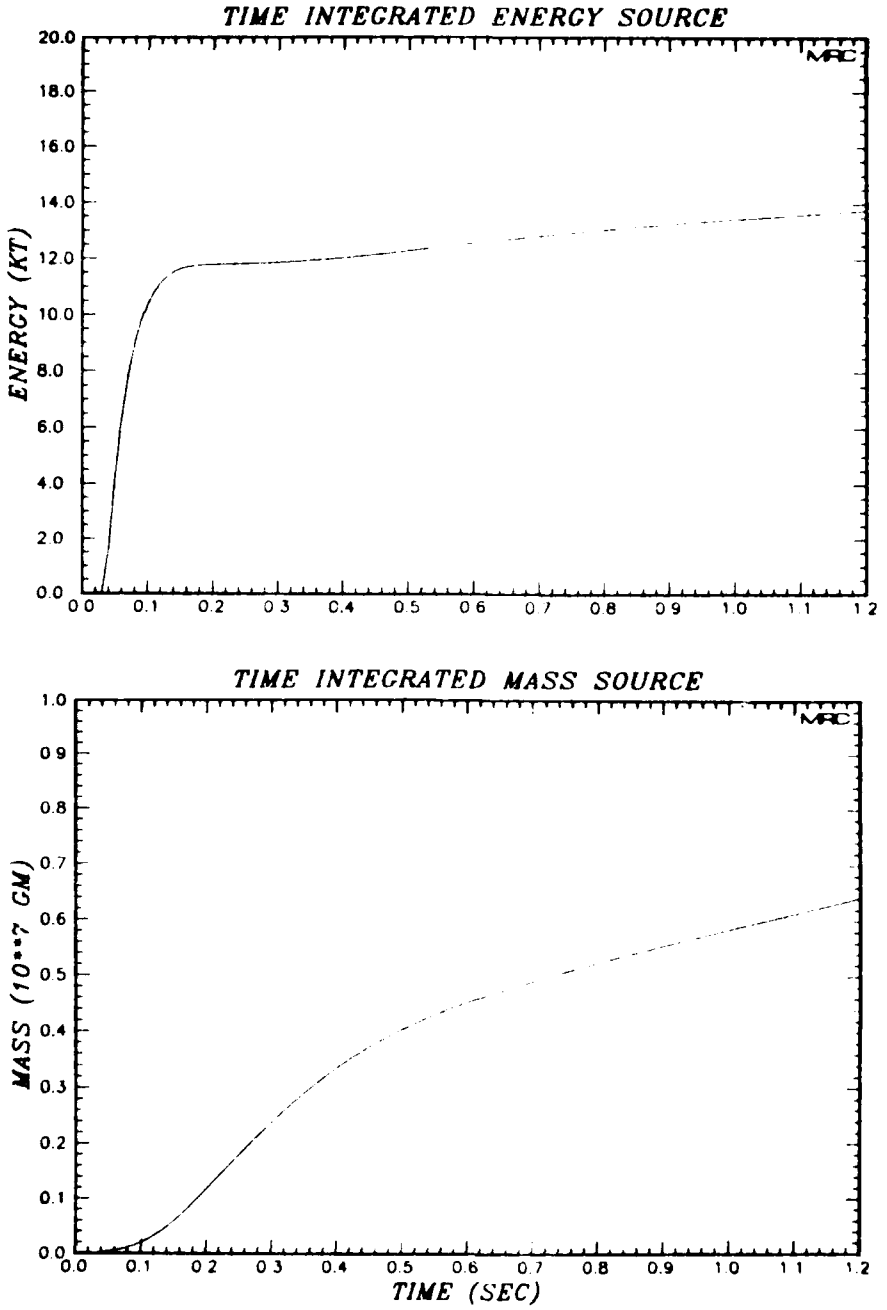

Figure 13. Time integrated values of the energy and mass sources.

About 90% of the energy is added by .10 seconds, and the remaining 10% is added slowly over the next 1.1 seconds. There is a peak in the rate of increase of ion mass at .2 seconds, but it is much less pronounced than the peak in the energy source function, resulting in a more gradual increase in mass over the running time of the problem. It is worth noting that the flux tube mass increases from about 1×10^5 gm (ambient ionosphere plus ionization produced by the X-ray flash) to about 60 times this value by 1.2 seconds. As we will see later, this is a very important aspect of the phenomenology of this burst.

Having obtained the flux tube geometry and the sources of energy and mass from the output of the full CMHD calculation, we then did a series of simplified "CMHD-like" calculations, in which we exercised the SCATTER subroutine to transfer energy from transverse thermal into parallel streaming energy, and the TRANSPORT subroutine to transport ions along the distorted field lines to the upper and lower ends of the flux tube.

The block diagram of Figure 14 illustrates schematically the flow of energy and mass in these simplified calculations. As energy is added, it first appears as transverse thermal energy. Then, provided the turn-on conditions for the particular "scattering instability" being modelled are met, the SCATTER subroutine illustrated by S in Figure 14 shifts ions in parallel velocity space, from small $U_\parallel$ and large $U_\perp$ into larger $U_\parallel$ and smaller $U_\perp$. This results in a transfer of energy from $E_\perp$ to $E_\parallel$. Ions with non-zero $U_\parallel$ then stream up or down the flux tube. This latter part of the calculation is the job of the TRANSPORT subroutine, illustrated in Figure 14 by the symbol T. In a particular sector, at a particular time, the amount of $E_\parallel$ present and its distribution in parallel velocity space are determined by the time integrated effects of the scattering process in that sector and transport between that sector and those above and below. This, in turn, determines whether or not the turn-on conditions for SCATTER are met.

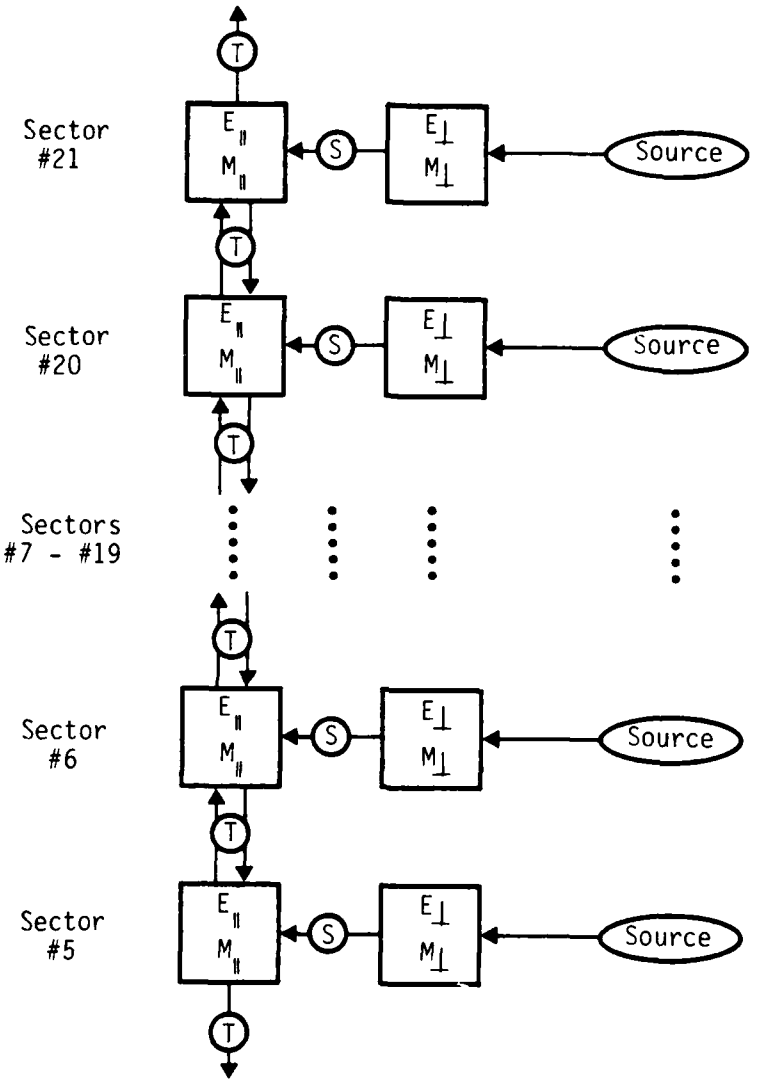

Figure 14. Schematic representation of the flow of energy and mass in the single flux table calculations. Angular sectors 5 through 21 are "active" for this flux tube - sectors 1 and 22 are straight down and straight up, respectively, where the non-orthogonality of the CMHD coordinate system causes singularities, and sectors 2 through 4 intersect this particular flux tube below the bottom of the CMHD grid. (S) represents the action of the SCATTER subroutine, which takes energy from transverse thermal and puts it into parallel streaming, and (T) represents the transport of parallel streaming energy up and down the flux tube.

The series of calculations being reported here was done to investigate the sensitivity of the patch spectrum to the details of the particular plasma instability model encoded in the SCATTER subroutine. Results from eight problems, which involved variations of two different instability models, are shown below.

The ions that reside in a particular spatial location, that is, in a particular angular sector of a given flux tube, are resolved into fifteen groups in parallel velocity space, covering the range from +4000 km/sec to -4000 km/sec. Velocities parallel to $\vec{B}$ are considered positive, antiparallel velocities are negative (the undistorted $\vec{B}$ field pointed downward, as at the geomagnetic north pole). Initially all the ions within a cell are in the $U_{\parallel} = 0$ group, as shown in Figure 15. As the ion mass within a cell increases due to collisional ionization of background air, the added ions also appear in the zero velocity group. Then, if the instability turn-on condition permits, ions are "scattered" from $U_{\parallel} = 0$, into both positive and negative values of $U_{\parallel}$, according to the particular scatter model being used. The two types of models used here are the diffusive scatter model, which produces a distribution function such as that shown in Figure 16, and the Workman-Palmadesso (WP) model, which preferentially scatters high velocity ions into the parallel direction, as is illustrated in Figure 17.

Figures 15 through 17 are plots of ion mass per unit velocity as a function of parallel velocity for one angular sector within a flux tube. By combining this information for all the active sectors, we can plot contours of ion mass per unit velocity as a function of parallel velocity and angular sector, resulting in displays such as shown in Figure 18. The detailed results of the present calculations can best be summarized by a sequence of plots like Figure 18, and a series of these plots at succeeding times for each of the eight calculations will be shown below.

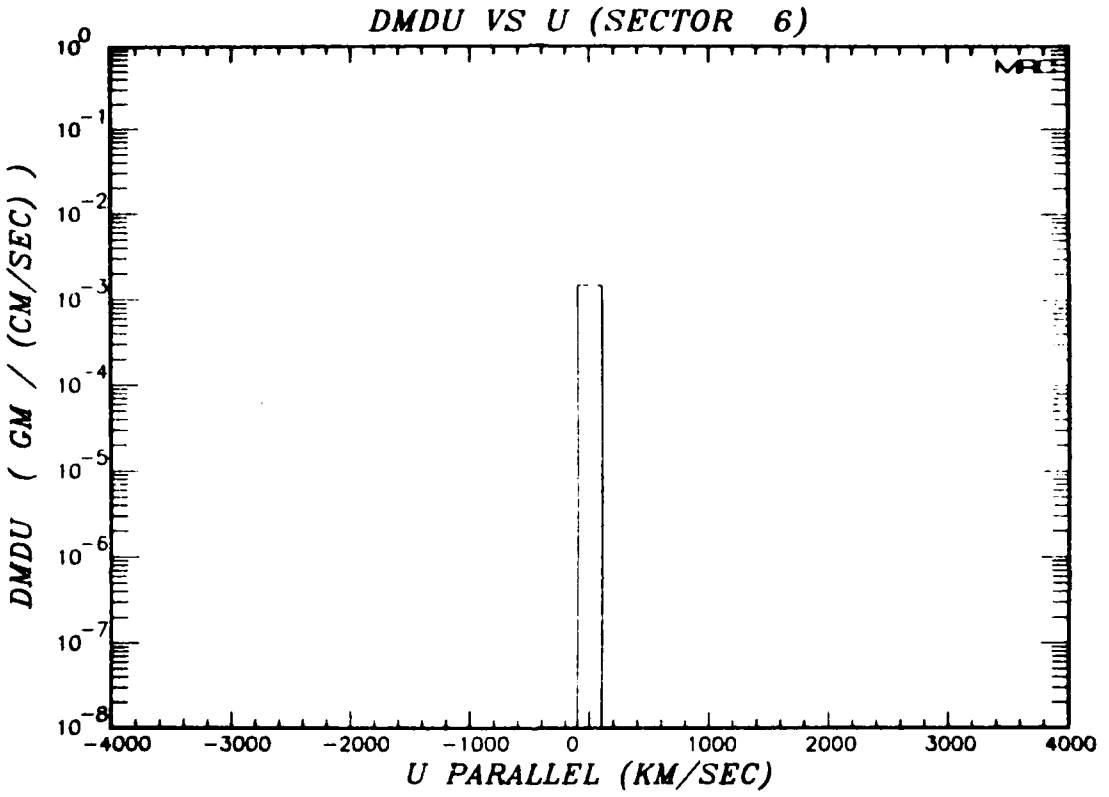

Figure 15. An example of the initial ion distribution function, $\frac{dM}{dU_{\parallel}}$, within one angular sector.

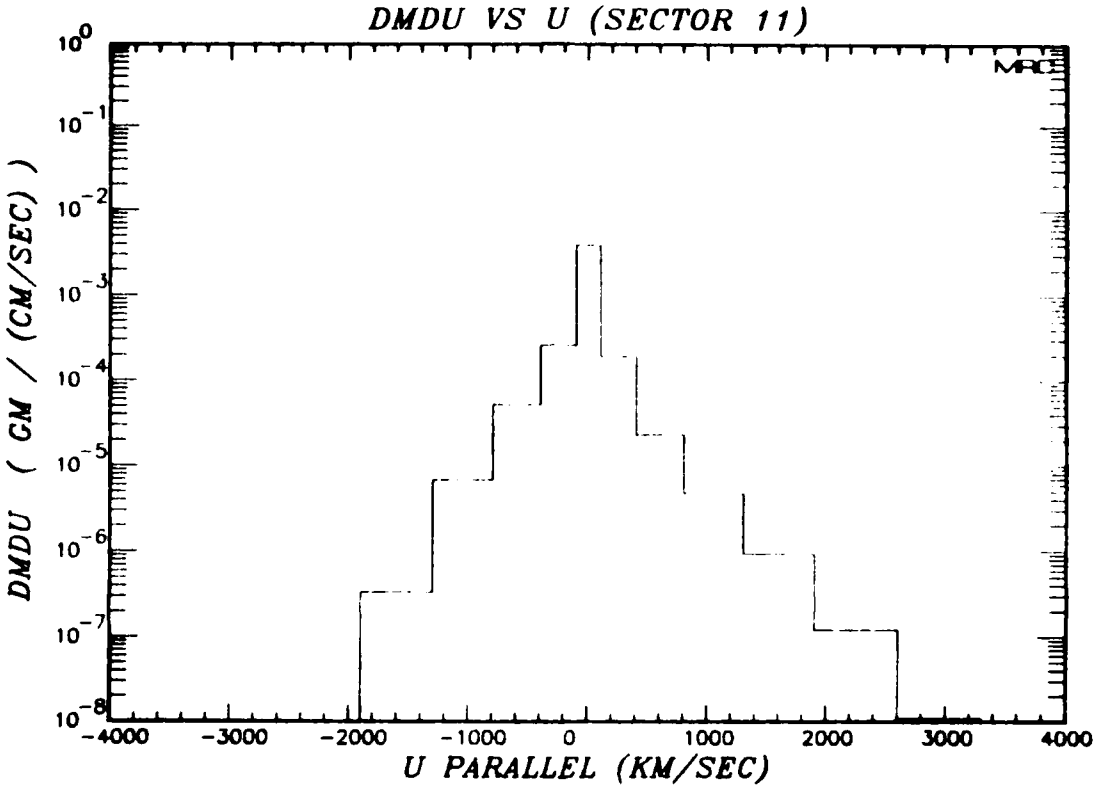

Figure 16. An example of the distribution function, $\frac{dM}{dU_{\parallel}}$, within one angular sector, after the diffusive SCATTER subroutine has deflected energy from the transverse direction into the parallel direction.

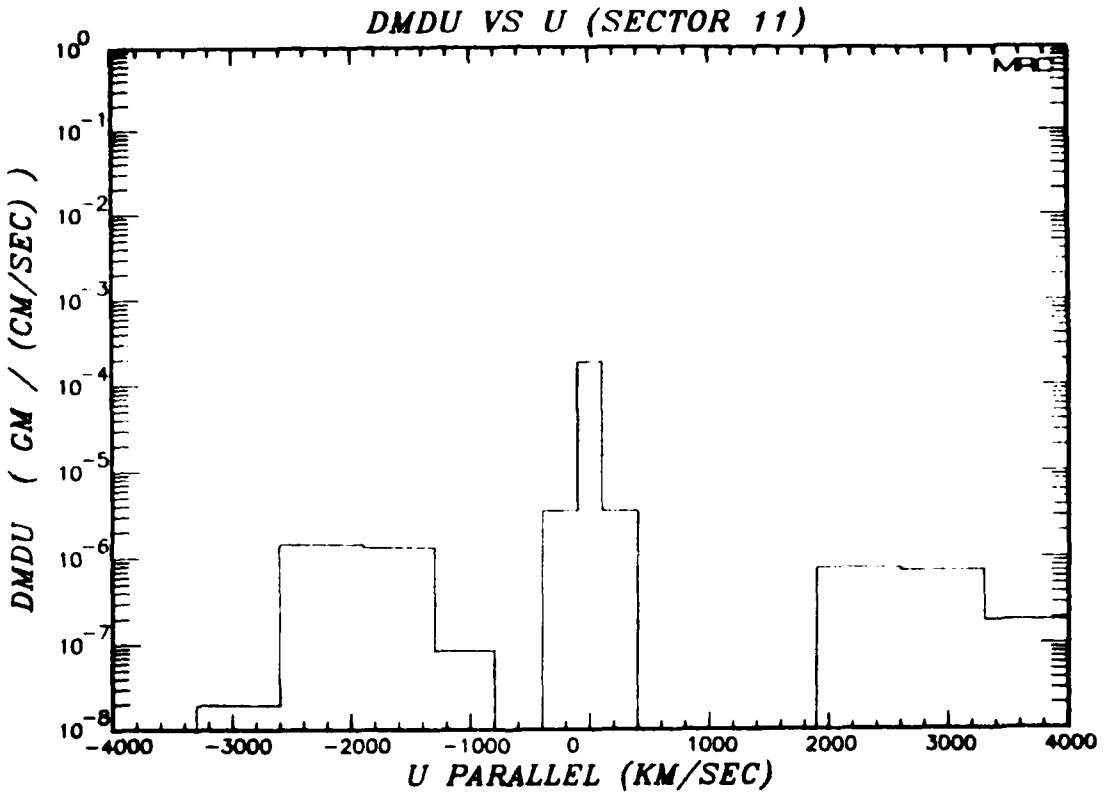

Figure 17. An example of the distribution function, $\frac{dM}{dU_{\parallel}}$, after the WP SCATTER routine has deflected energy from the transverse direction to the parallel direction.

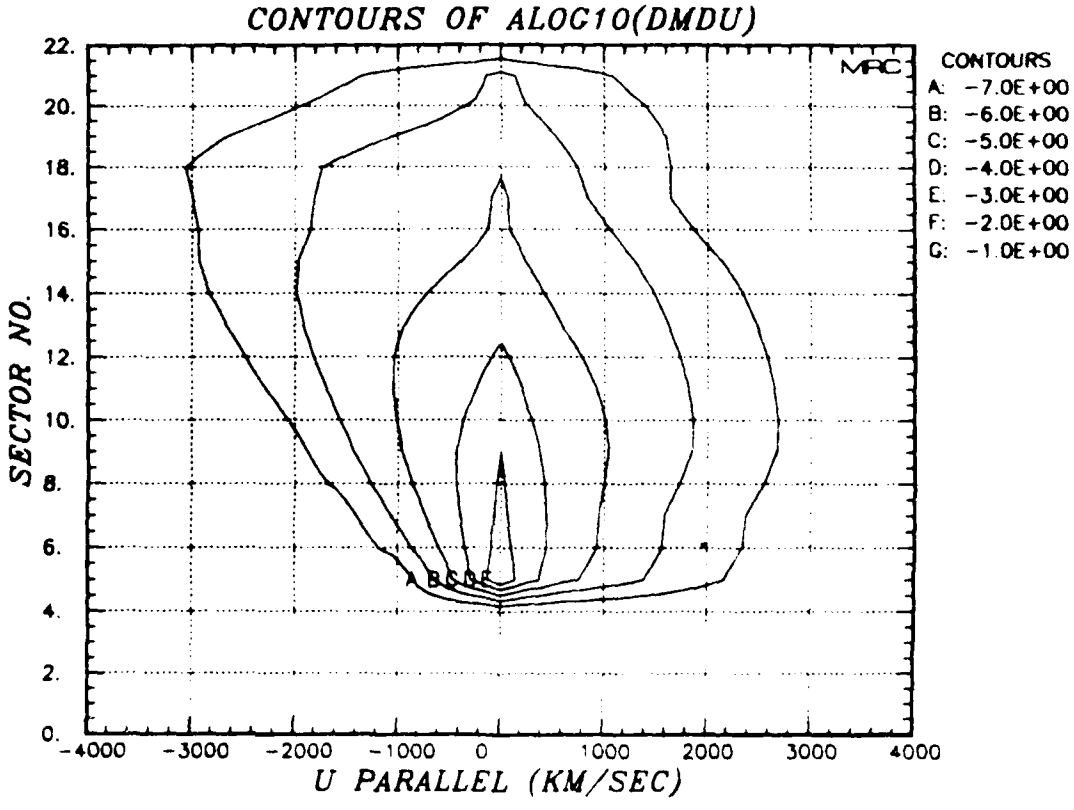

Figure 18. Typical contours of the logarithm of the distribution of ion mass per unit parallel velocity, with $dM/dU_{\parallel}$ in units of gm/(cm/sec), as a function of parallel velocity and angular sector number. The outermost contour has $dM/dU_{\parallel} = 10^{-7}$ gm/(cm/sec), and the innermost contour has $dM/dU_{\parallel} = 10^{-3}$ gm/(cm/sec) in this example at a time of 0.1 sec.

With this introduction, then, we proceed to present results from the eight calculations. The first calculation, which we shall call CASE 1, used the diffusive form of scattering function, which performed a simple diffusion in velocity space, whenever the mean parallel thermal energy per ion was less than one-half the mean transverse thermal energy per ion. That is, the turn-on condition was

$$e_{\parallel} < 0.5\, e_{\perp},$$

with
$$e_{\parallel} \equiv \frac{\sum 0.5\, m_k (U_{\parallel k} - \bar{U}_{\parallel})^2}{\sum_k m_k},$$

where
$$\bar{U}_{\parallel} \equiv \frac{\sum m_k\, U_{\parallel k}}{\sum_k m_k}\ .$$

The summations are, of course, over the 15 parallel velocity groups. The time scale for the diffusion, or scattering, was short compared to other times of the simulation, so that the value of $e_{\parallel}$ was nearly always at least as large as it would be for complete isotropization.

Figure 19 contains plots of the total transverse thermal energy in the flux tube, the total parallel energy, and the energy transported out the ends of the flux tube as functions of time. The transverse energy peaks at about .15 seconds, thereafter falling gradually, as energy is scattered into the parallel direction at a faster rate than it is being increased by continuing compression of the flux tube. The parallel energy rises somewhat less rapidly than does the transverse, peaking at about .2 seconds, and then stays fairly constant. This points out an important property of this system, namely, that since the plasma instability time scale is very short compared to other time scales in the problem, energy is scattered into the parallel direction at whatever rate is required to maintain a quasi-equilibrium between the scattering process and transport

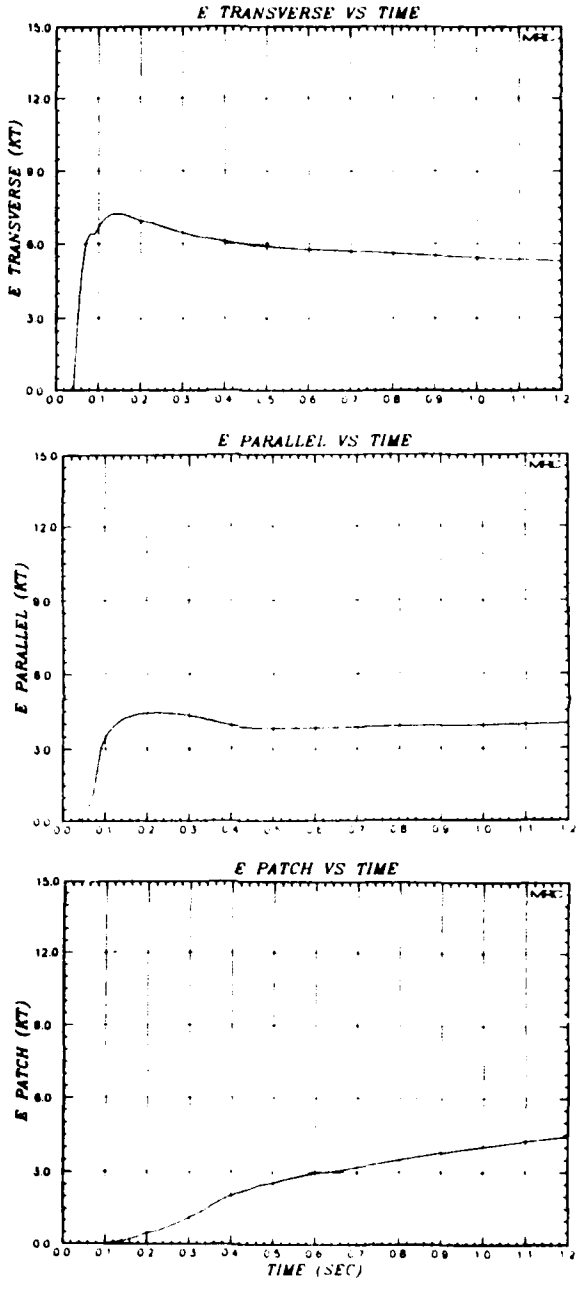

Figure 19. Transverse energy, parallel energy, and patch energy as functions of time for CASE 1.

of parallel energy up and down the flux tube. That is, the rate of transport - determined by the geometry of the flux tube and the distribution of energy in parallel velocity space - is the controlling rate. The third graph in Figure 19 gives the energy which has been transported out the top and bottom of the grid, and subsequently would be deposited in the patch regions, as a function of time. It rises somewhat more steeply at first, when the fastest ions are exiting the flux tube, and somewhat less steeply later. The maximum slope occurs at about 0.3 seconds, which agrees with the time of the peak in the power-time curve inferred from optical data.

As a way of displaying the evolution of this problem in more detail, we show contour plots of the distribution function $dM/dU_{\parallel}$ at several times in Figures 20 and 21. The problem was initialized at .025 seconds, and the correponding ion mass distribution function is strongly peaked at $U_{\parallel} = 0$. The peak is highest in sector 5, which is at the lowest altitude and therefore contains the most X-ray-produced ionization. The contour values are a factor of ten apart, and the contours which appear at this time range from the 1×10^{-7} gm/(cm/sec) to 1×10^{-3} gm/(cm/sec). At subsequent times, as mass and energy are added, and as the diffusive SCATTER routine is turned on, the distribution function is spread out in $U_{\parallel}$ space, and the peak value increases. At .050 seconds, the plot is fairly symmetric about $U_{\parallel} = 0$, due to the symmetry of the SCATTER algorithm, and the limited amount of elapsed time since most of the scattering has occurred. By the next time, however, ion transport has moved those particles with anti-parallel (upward) velocities to higher angular sectors, and those with parallel (downward) velocities to lower sectors, producing a skewing of the contours. By .20 seconds, the skewing has become more pronounced. At progressively later times, the skewed nature persists, but the contours retract toward the center as the faster particles are transported out the ends of the flux tube. As this is taking place, the SCATTER routine continues to diffuse ions in parallel velocity space as needed to keep $e_{\parallel}$ up to the "turn-on" value. However, as mass is added - the

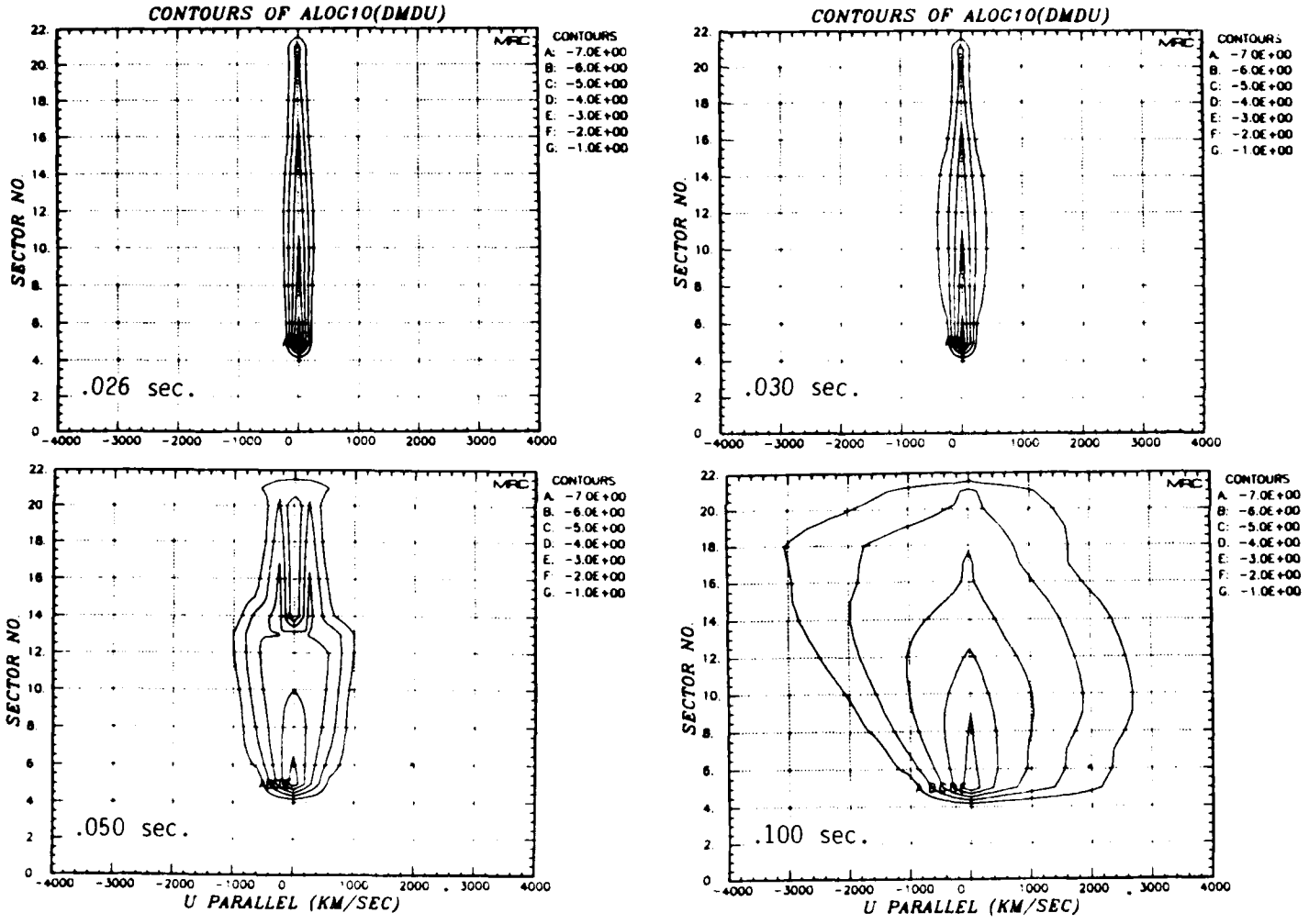

Figure 20. Distribution function contours for CASE 1 at times of .026, .030, .050, and .100 seconds.

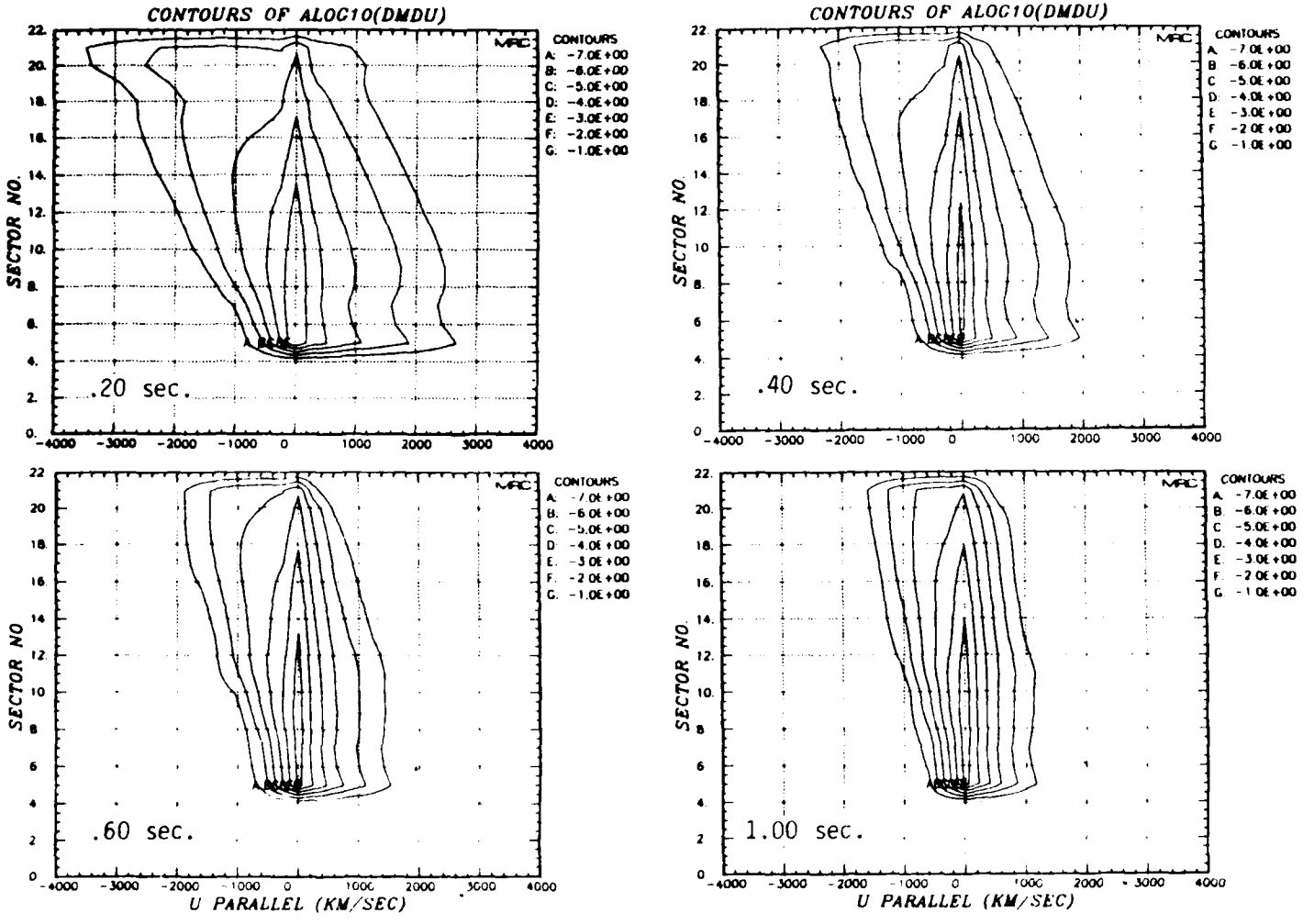

Figure 21. Distribution function contours for CASE 1 at .20, .40, .60, and 1.00 seconds.

total ion mass increases 60-fold during the course of the problem - the average transverse energy per ion becomes smaller, lowering the necessary spread of ions in $U_{\parallel}$ space. At 1 second, the mass in the problem has increased so that the contours range from 1×10^{-7} gm/(cm/sec) to 1×10^{-2} gm/(cm/sec). The calculation was continued to a problem time of 2 seconds, at which time the simplifying assumption was made that any further evolution of the distribution function would be due solely to transport. We could then construct the time-integrated patch spectra for both the upward - and downward - going ions. Figure 22 shows the spectrum for the downward patch, which has a shape characteristic of CMHD results, approximately proportional to $U_{\parallel}^{-1}$.

CASE 2 utilized the WP SCATTER algorithm, which is quite different from the diffusive one. Rather than simply spreading the distribution function out in $U_{\parallel}$ space, it deflects ions directly out to parallel velocities given by $\pm \lambda V_{\perp th}$, where the NRL recommended value of λ is 2.5, and $V_{\perp th}$ is the mean transverse thermal velocity of the ions in that spatial location. The total transverse, parallel, and patch energies as functions of time are plotted in Figure 23. Figures 24 and 25 given contours of the distribution function as it evolves for this case. The effects of the WP SCATTER algorithm are quite obvious, particularly at times of .05, .10, and .20 seconds. The scattering of ions out to $U_{\parallel} = \lambda V_{\perp th}$, coupled with a $V_{\perp th}$ that increases with altitude gives a "winged" appearance to the contour plots at .05 and .10 seconds. At the later times, after the faster ions have had time to be transported out of the flux tube, these effects are less obvious. The resulting patch spectrum is shown in Figure 26.

CASE 3 used a combined SCATTER algorithm, that both diffused ions in velocity space and deflected ions directly out to $\pm \lambda V_{\perp th}$. The other five cases used variations of the WP algorithm. Table I lists the

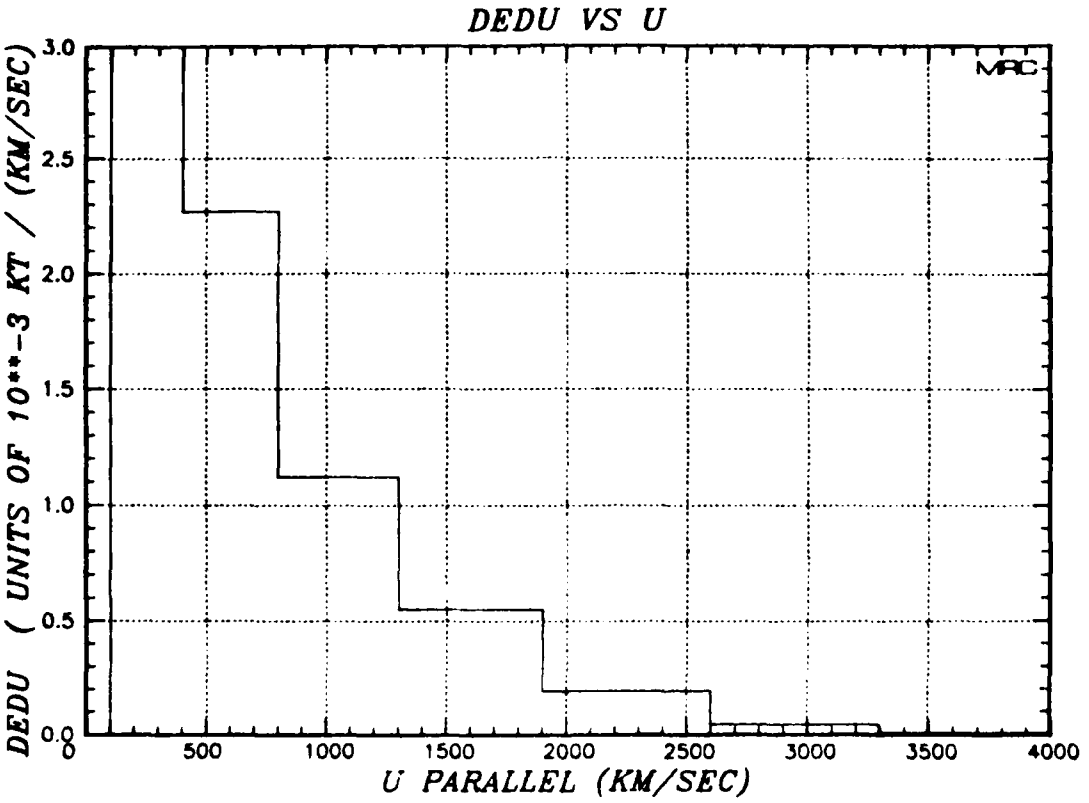

Figure 22. The velocity spectrum, $\frac{dE}{dU_{\parallel}}$, for the downward patch for CASE 1.

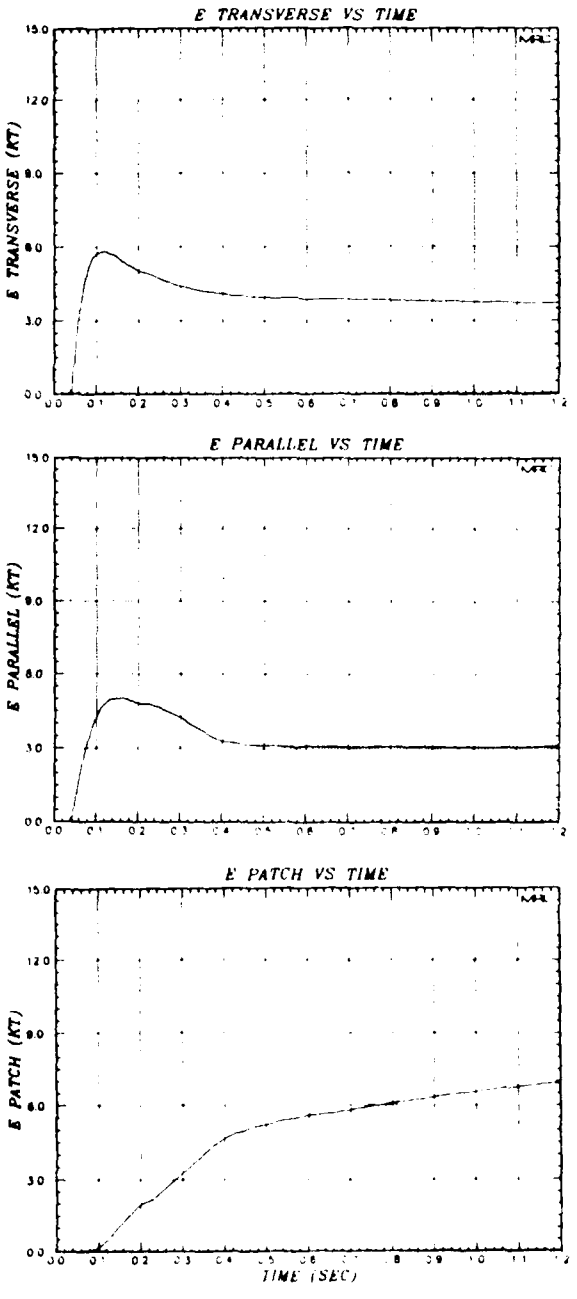

Figure 23. Transverse energy, parallel energy, and patch energy as functions of time for CASE 2.

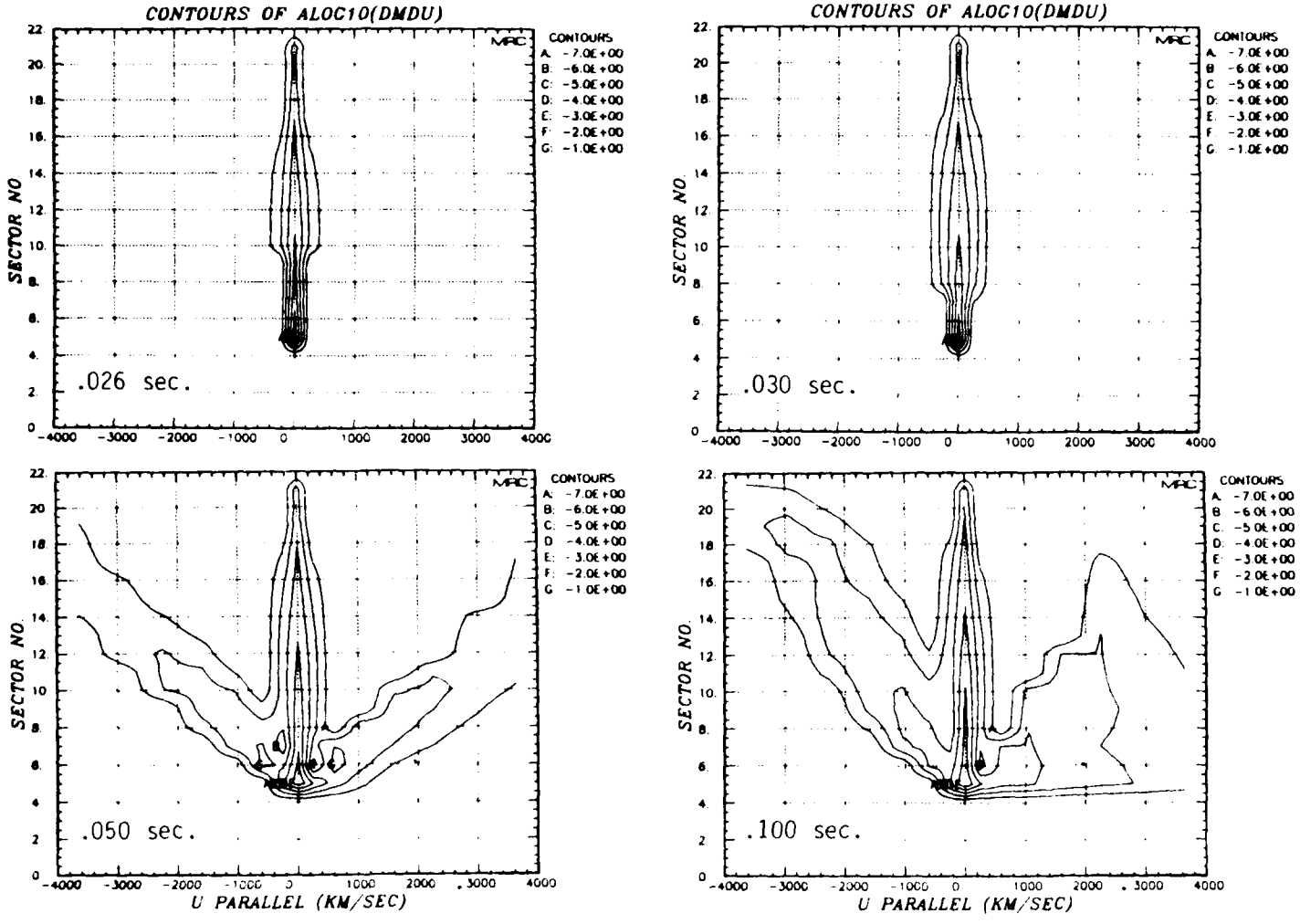

Figure 24. Distribution function contours for CASE 2 at times of .026, .030, .050, and .100 seconds.

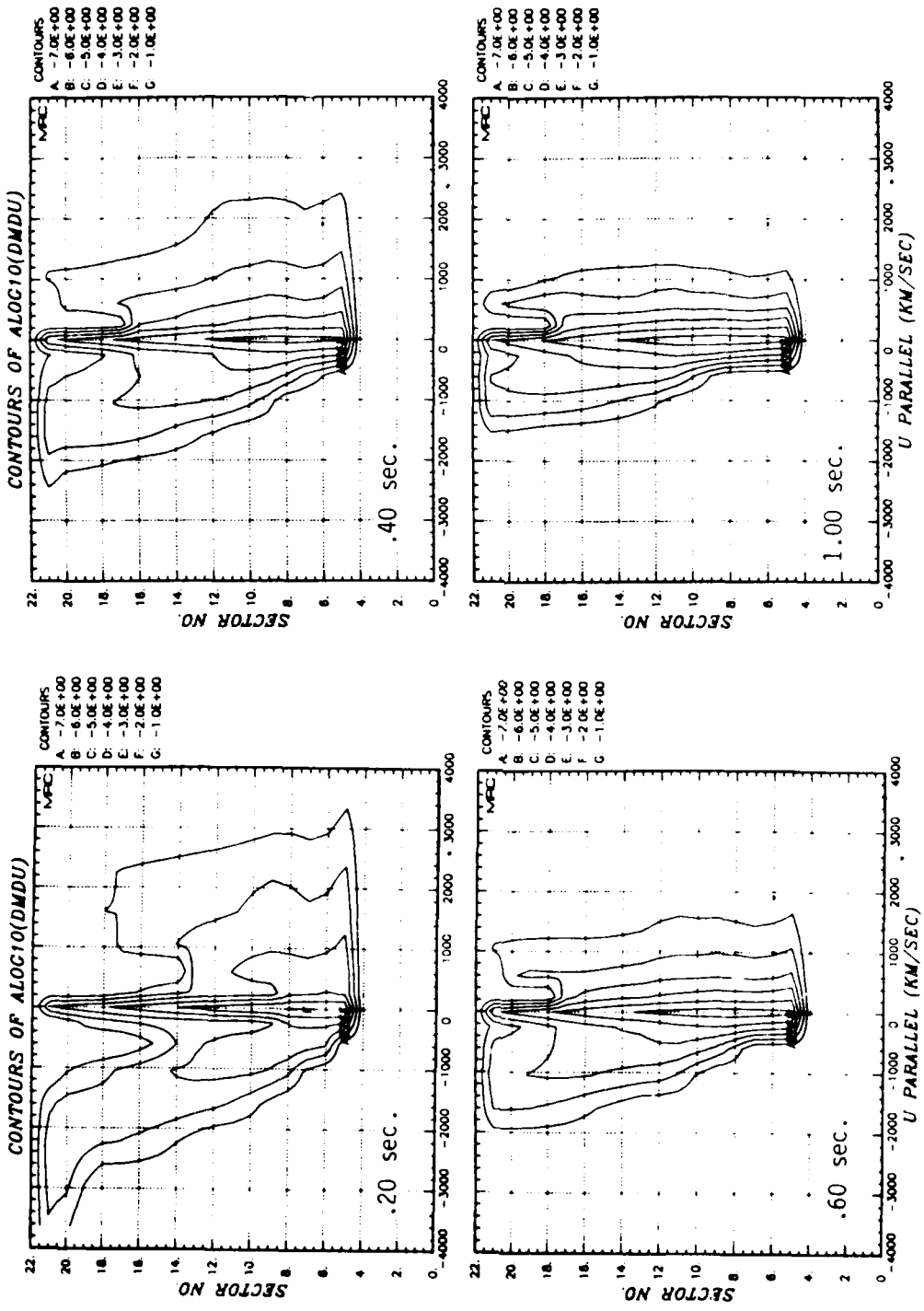

Figure 25. Distribution function contours for CASE 2 at times of .20, .40, .60, and 1.00 seconds.

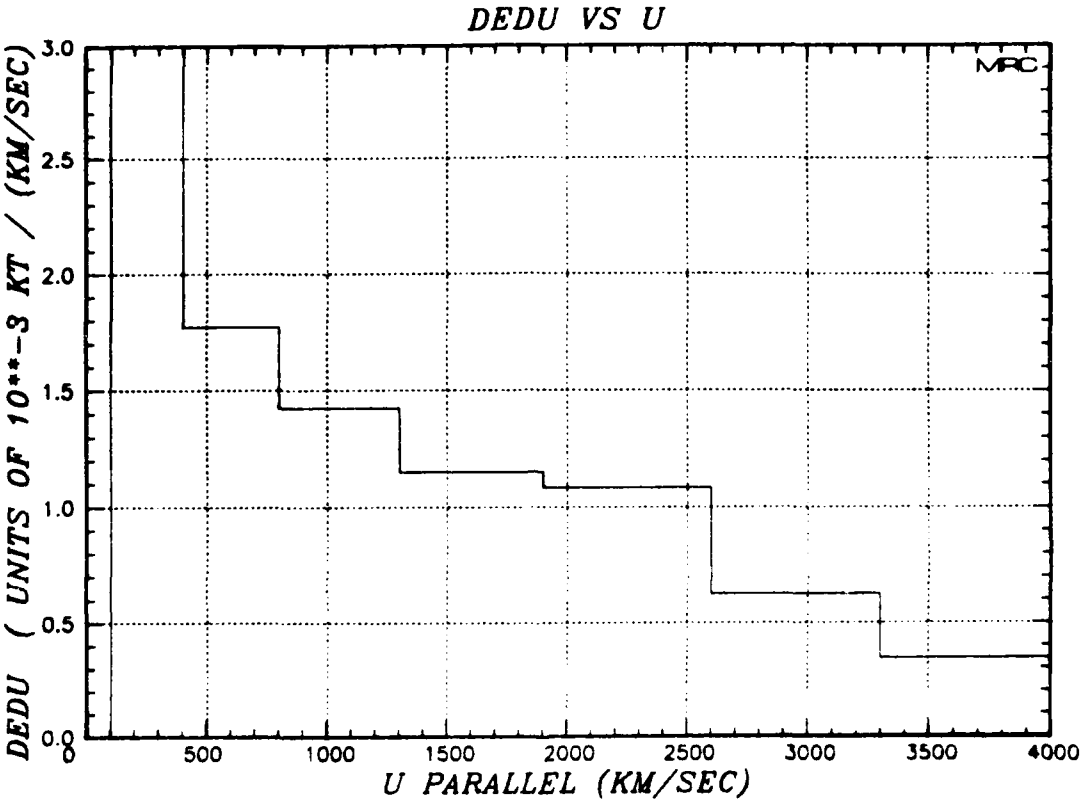

Figure 26. The velocity spectrum, $\frac{dE}{dU_{\parallel}}$, for the downward patch for CASE 2.

Table 1. Parameters used for the eight different single flux tube calculations

	Type	Value of λ	Turn-on Conditions	f_{mass}
Case 1	Diffusive	N.A.	$e_{\parallel} < .5\ e$	1.0
2	WP	2.5	$e_{\parallel} < .5\ e$	1.0
3	WP + Diffusive	2.5	$e_{\parallel} < .5\ e$	1.0
4	WP	2.5	$e_{\parallel} < 10\ e$	1.0
5	WP	5.0	$e_{\parallel} < .5\ e$	1.0
6	WP	2.5	$e_{\parallel} < .5\ e$	.10
7	WP	2.5	$e_{\parallel} < .5\ e$	.01
8	WP	2.5	$e_{\parallel} < .5\ e$	0

eight runs, the type of scatter algorithm used, the value of λ, the turn-on condition, and the value of f_{mass}, a parameter by which the rate of addition of ion mass was multiplied.

Comparisons of the results of CASE 2, CASE 3, CASE 4 and CASE 5 are made in Figures 27 through 33. CASE 2 is the nominal WP scatter run, while CASE 3 includes some velocity diffusion. CASE 4 differed from CASE 2 in that the turn-on condition was altered to allow almost all (~ 90%) of the available thermal energy to be deflected into parallel energy. CASE 5 was different from the nominal case in that a larger value for λ was used, thus deflecting ions to higher parallel velocities for a given V_{th}. Time histories of transverse thermal energy ($E_{\perp}$) for the four cases are plotted in Figure 27. The CASE 2 and CASE 3 plots are very similar. The plot for CASE 4 shows that relatively little energy was left in $E_{\perp}$, since most of it went into parallel energy. CASE 5 has less $E_{\perp}$ than the

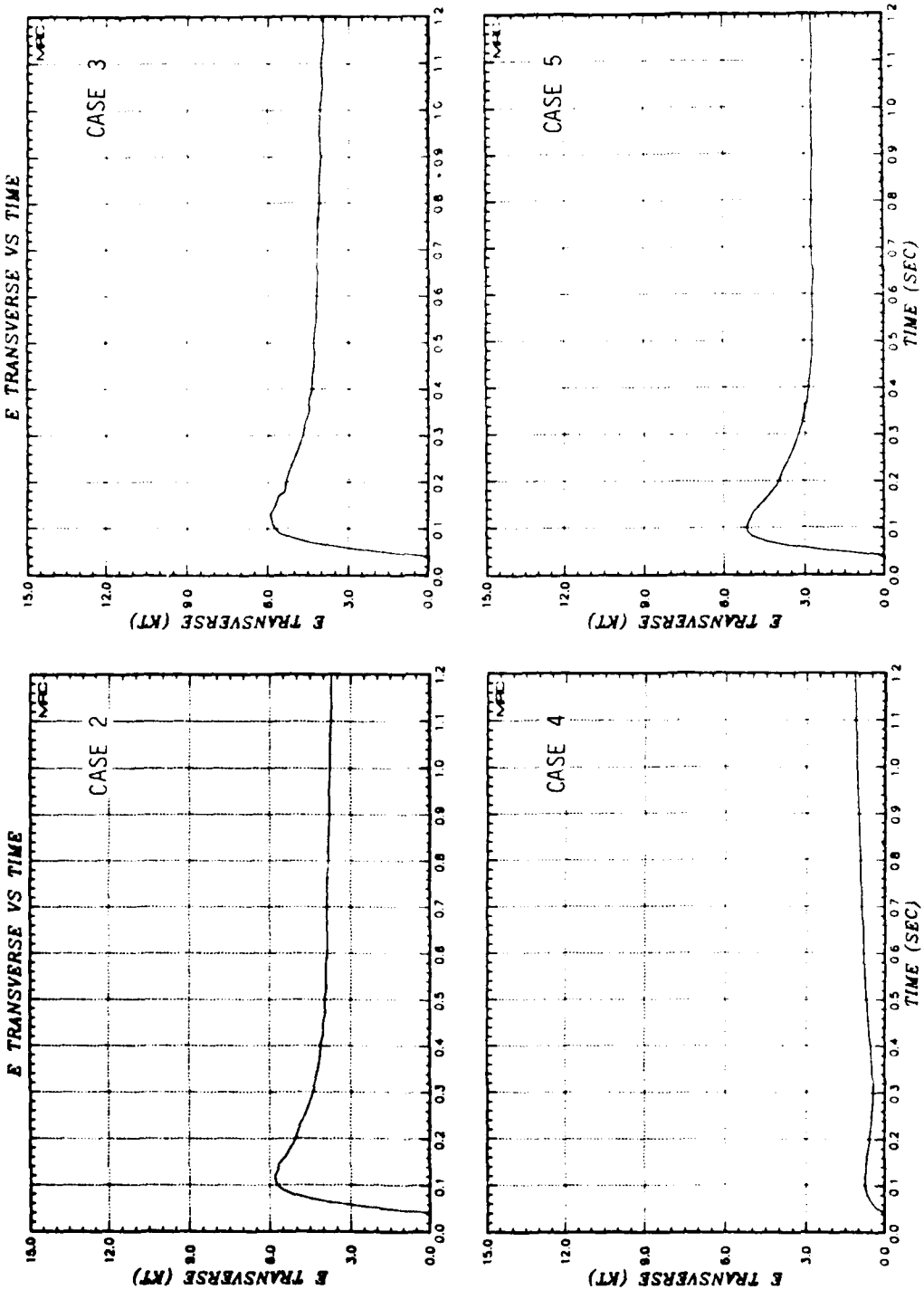

Figure 27. Transverse energy as a function of time for CASE 2, CASE 3, CASE 4, and CASE 5.

first two, because deflecting ions to higher parallel velocities results in energy being transported out of the flux tube at a faster rate, thereby requiring a higher rate of conversion of energy from $E_\perp$ to $E_\parallel$.

Parallel energies are plotted for the four cases in Figure 28. Again, CASE 2 and CASE 3 are very similar. CASE 4 shows substantially more $E_\parallel$ at first, but after about .5 seconds, it has about the same remaining parallel energy as the others. CASE 5 has slightly more $E_\parallel$ than the first two cases before about .3 seconds, and slightly less thereafter. This difference is not surprising, since CASE 5 deflected ions to higher values of $U_\parallel$, especially early in the problem, which subsequently increased the rate of transport out of the grid.

Figure 29 shows plots of patch energy vs. time. Again, the first two cases look very much alike. Cases 4 and 5 show a faster rate of delivery of energy to the patch at early times, which is consistent with the above discussion.

Contours of the distribution functions for the four cases at .05 seconds are presented in Figure 30. Here, we see a difference between cases 2 and 3. The latter, having employed a mixture of the diffusive and WP scattering algorithms, shows a broader distribution near $U_\parallel = 0$ than any of the others. CASE 4, which put essentially all of its energy into $E_\parallel$, clearly shows more ions in the 1000 km/sec to 3000 km/sec range than the other cases show. CASE 5, which deflected ions out to $U_\parallel = \pm 5\ V_{\perp th}$, shows more ions at the extremes of the velocity range. By .4 seconds, the time of the distribution function plots shown in Figure 31, there remain some differences between the various cases, but they are much less obvious than earlier. Figure 32 shows the 1 second comparison. At this time, the differences between the four cases are insignificant. We attribute the similarity in these plots to the fact that the energy and mass source

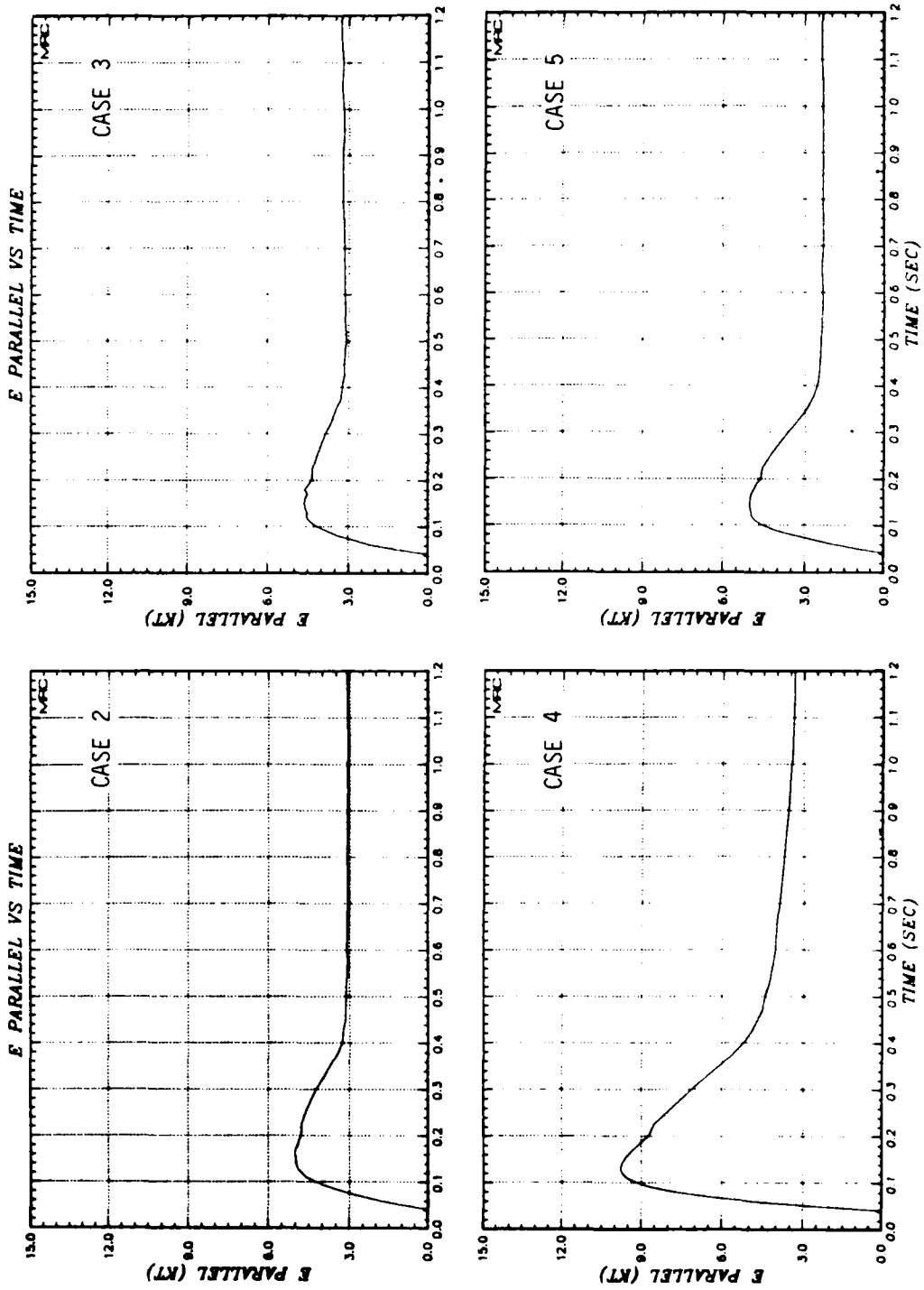

Figure 28. Parallel energy as a function of time for CASE 2, CASE 3, CASE 4, and CASE 5.

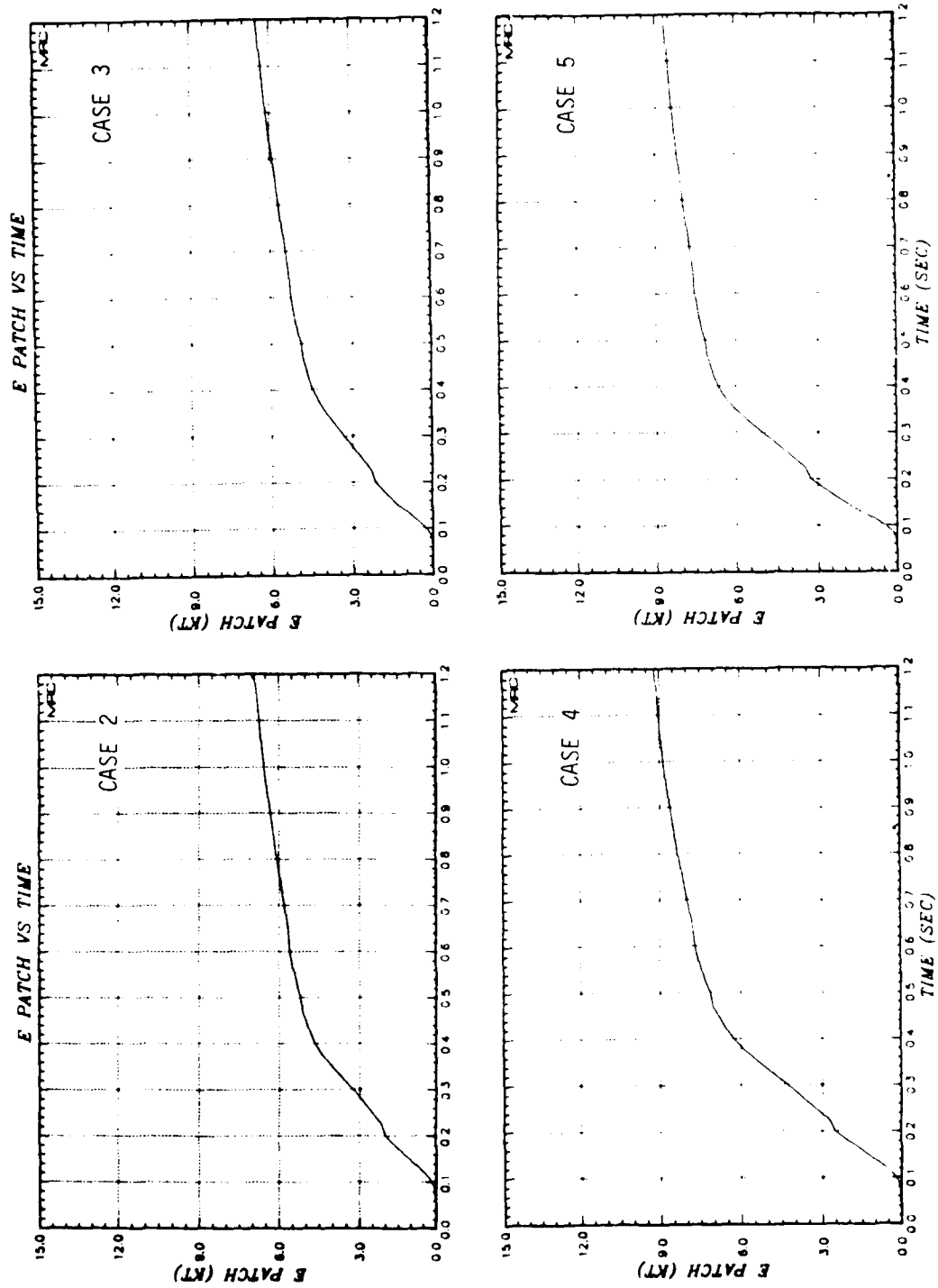

Figure 29. Patch energy as a function of time for CASE 2, CASE 3, CASE 4, and CASE 5.

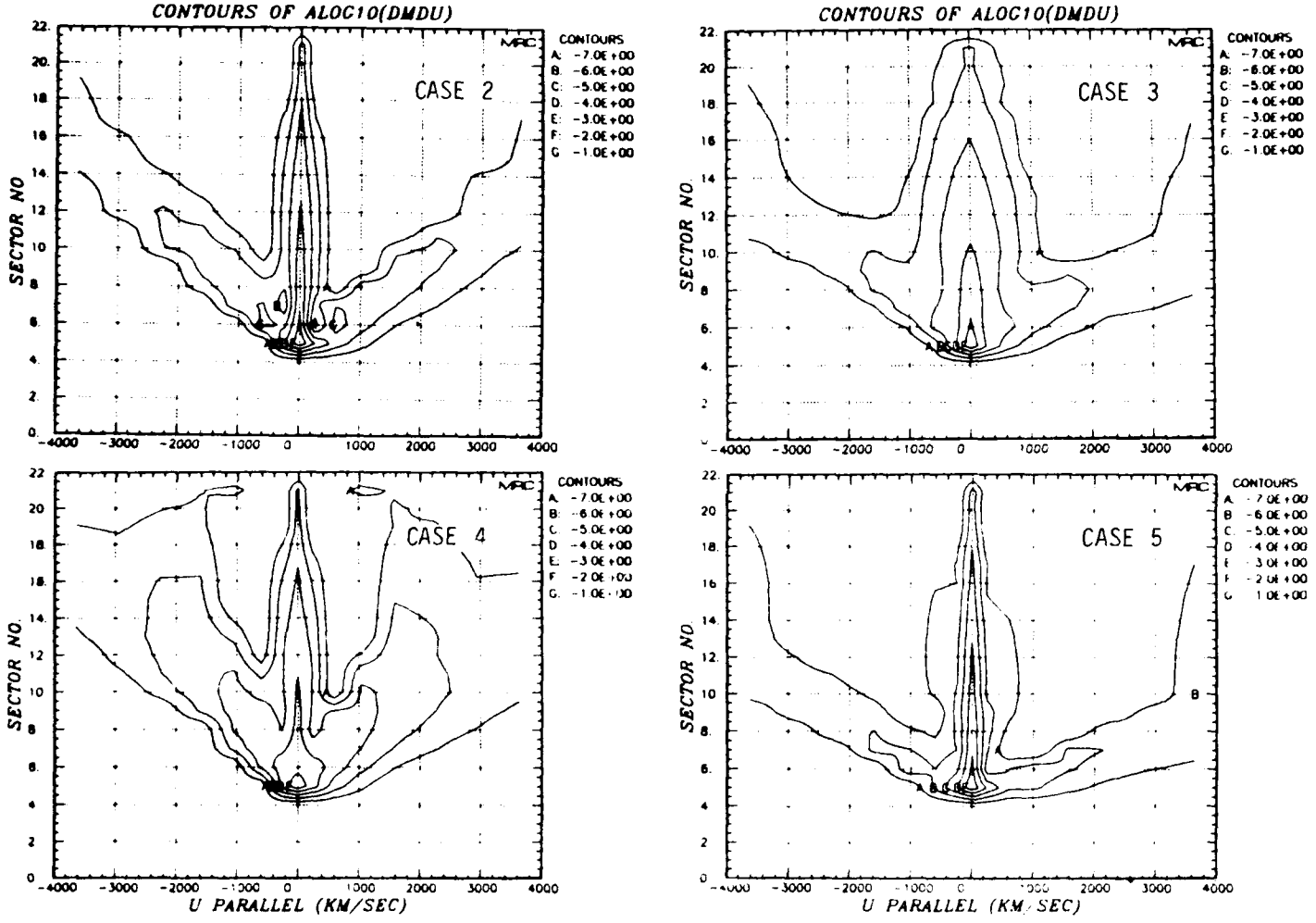

Figure 30. Comparison of distribution function contours for CASE 2, CASE 3, CASE 4, and CASE 5 at .05 seconds.

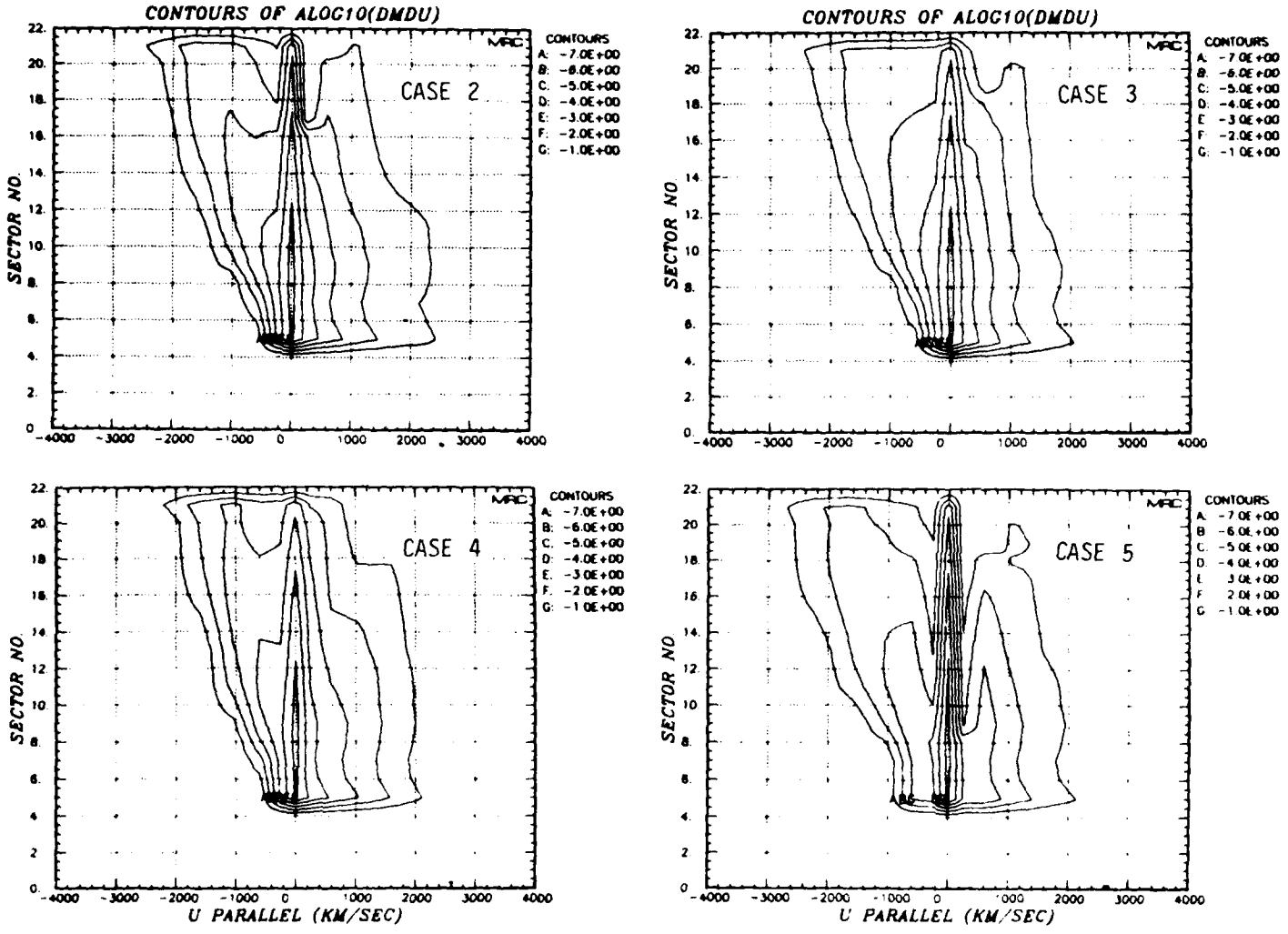

Figure 31. Comparison of distribution function contours for CASE 2, CASE 3, CASE 4, and CASE 5 at .40 seconds.

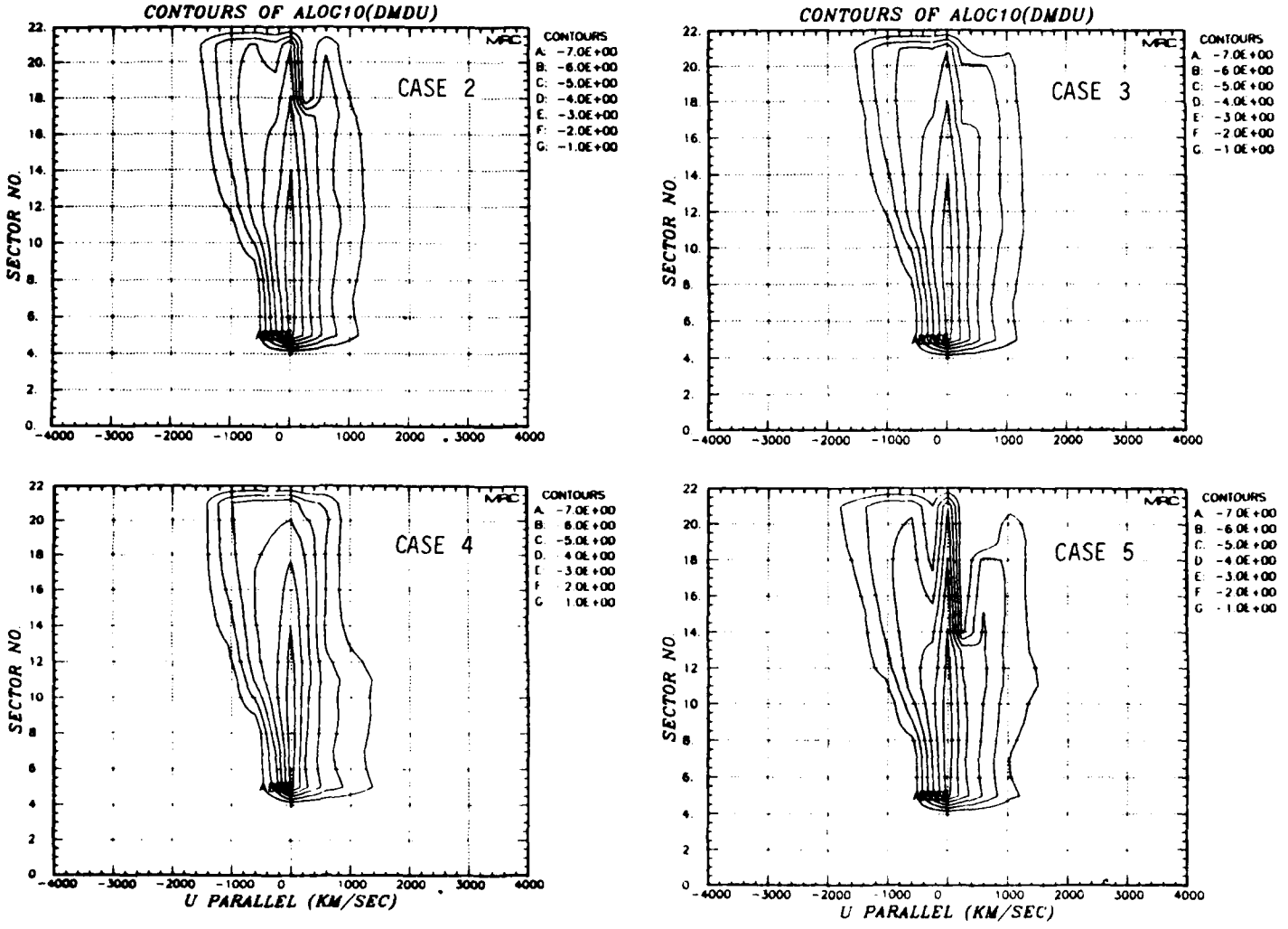

Figure 32. Comparison of distribution function contours for CASE 2, CASE 3, CASE 4, and CASE 5 at 1.0 seconds.

functions were the same for all cases, and to the fact that the controlling rate is that of transport, rather than the rate of scattering in velocity space. Thus the details of the scattering mechanism are not as critical as one might initially presume for times after 0.5 seconds when the low velocity patch ions are generated.

Figure 33 gives the patch spectra. The most significant differences occur at velocities above 3000 km/sec. Clearly, the amount of energy which reaches the conjugate regions at these high velocities depends on the plasma instability model used to deflect ions into the parallel direction. There are also differences in the low velocity (say, $\lesssim$ 1500 km/sec) portion of the spectrum, but they are less pronounced than at high velocities. The one thing these results have in common is that they all show a substantial low velocity component, and there is a definite trend for the energy per unit velocity to increase as the velocity decreases, for $U_{\parallel} \lesssim 2000$ km/sec.

The final comparison we shall make is between cases 2, 6, 7, and 8. These runs differ in the amount of ion mass added during the running of the problem. Of course, we are sure that CASE 2 has the appropriate amount of added ion mass, since we are confident that collisional ionization of background air really does occur, and that the cross-sections used are reasonably accurate. The purpose of this comparison is to demonstrate the importance of this aspect of the early time phenomenology.

Figures 34 through 36 show comparisons of $E_{\perp}$, $E_{\parallel}$, and E_{patch}. The shapes of the curves for the four cases are all quite similar. The differences indicate that as the rate at which mass is added is reduced, the rate of transport of energy out of the grid is increased, thus leaving progressively less energy in both $E_{\perp}$ and $E_{\parallel}$ for cases 6, 7, and 8 at comparable times. In Figures 37 through 39, we compare the distribution

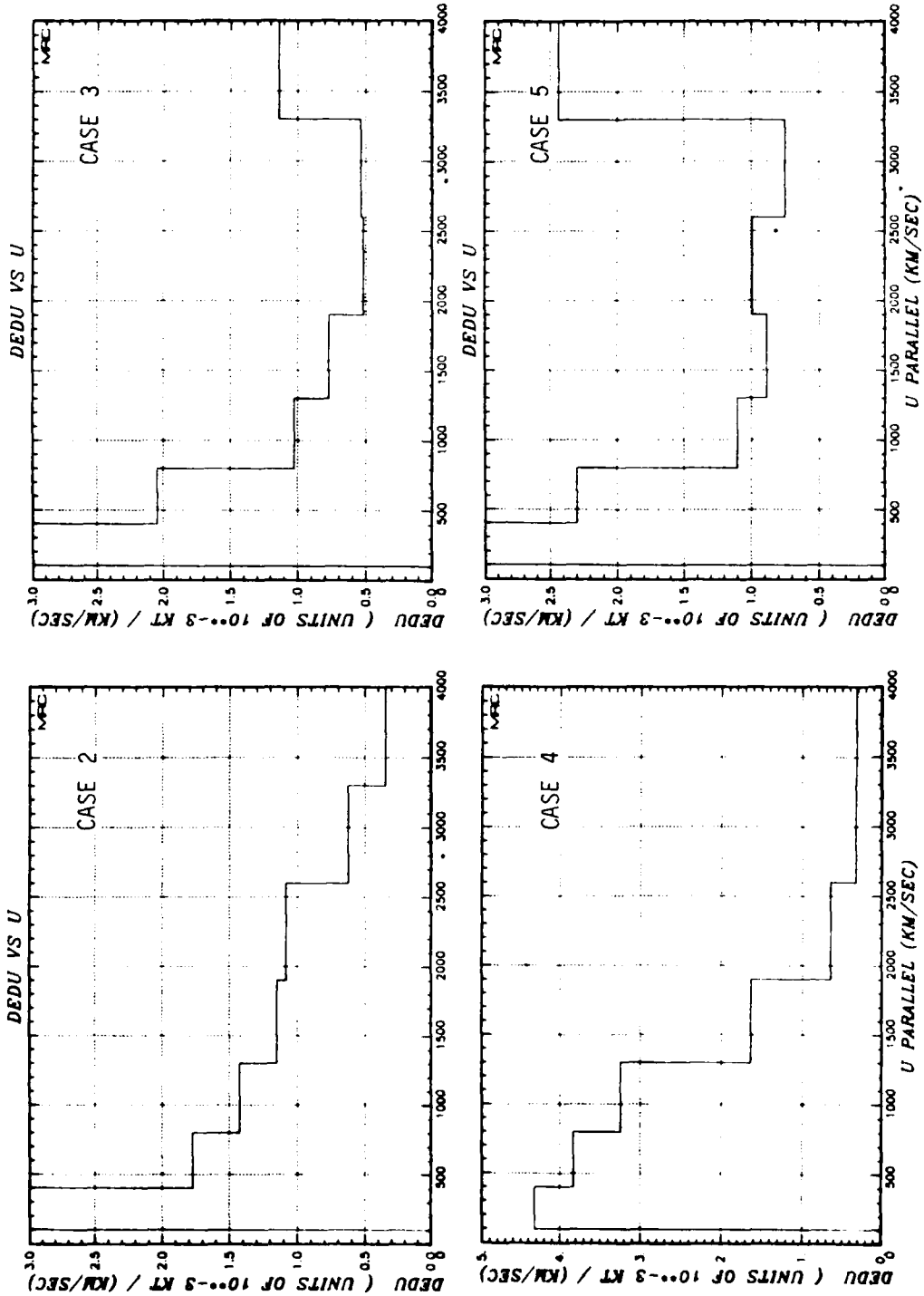

Figure 33. Comparison of patch spectra for CASE 2, CASE 3, CASE 4, and CASE 5.

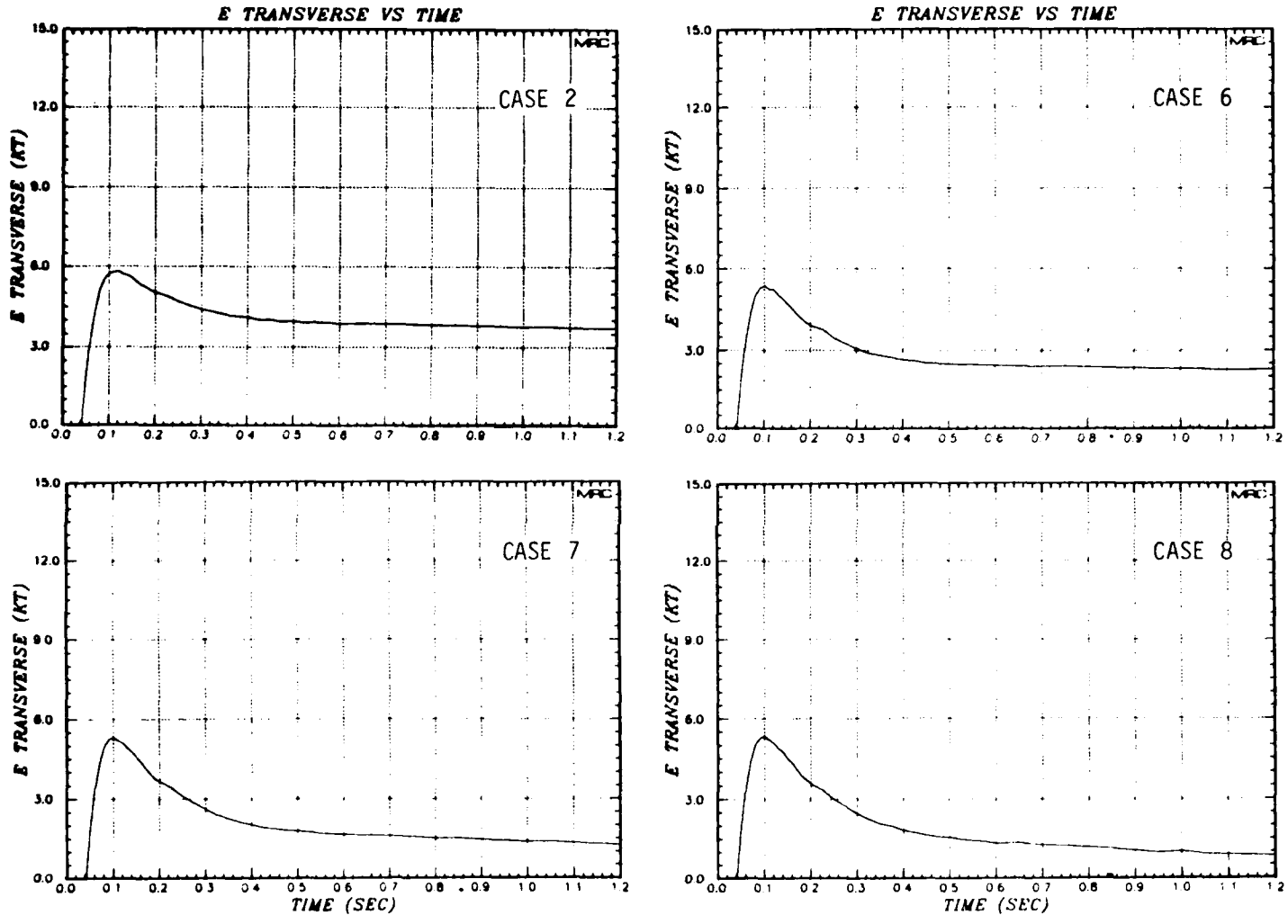

Figure 34. Transverse energy as a function of time for CASE 2, CASE 6, CASE 7, and CASE 8.

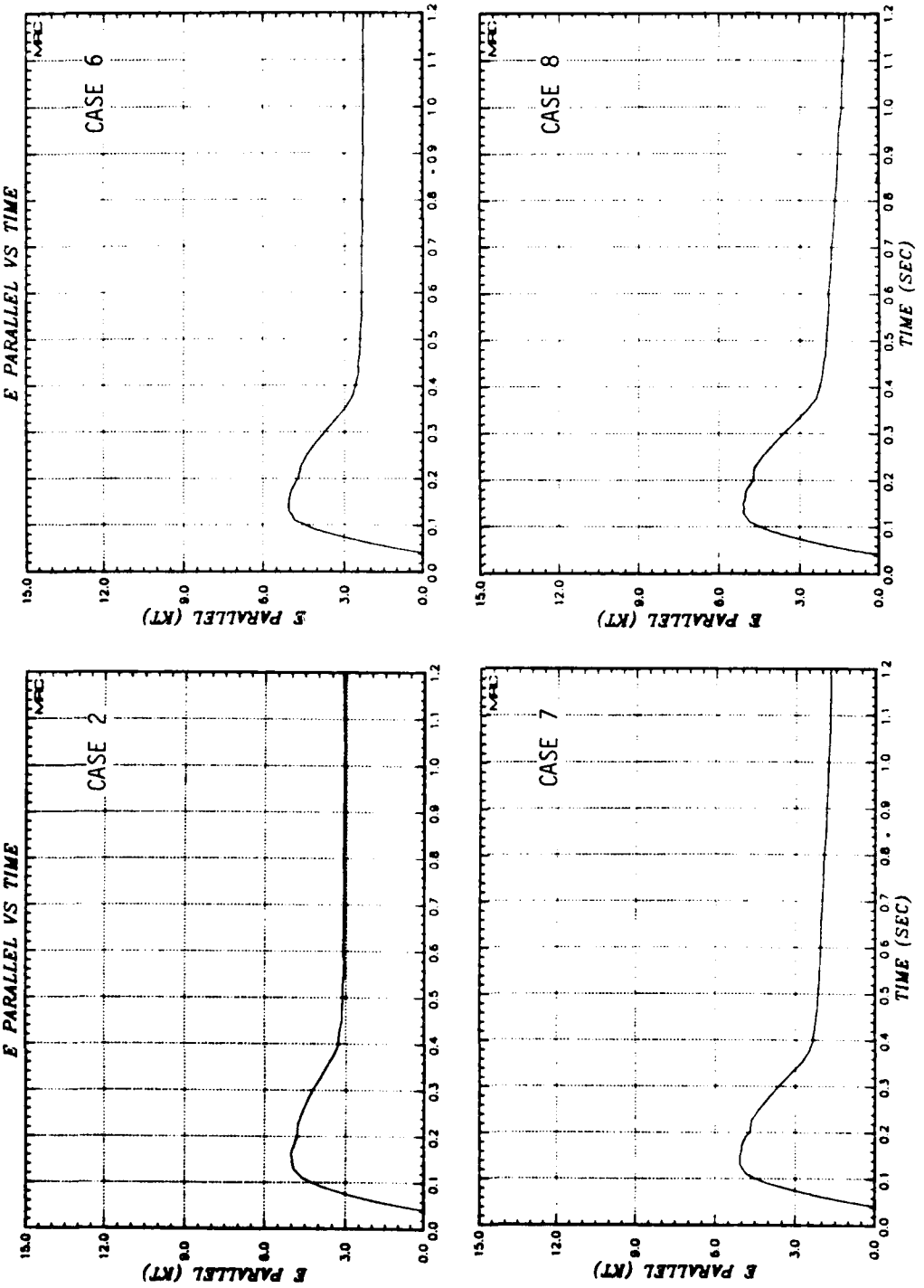

Figure 35. Parallel energy as a function of time for CASE 2, CASE 6, CASE 7, and CASE 8.

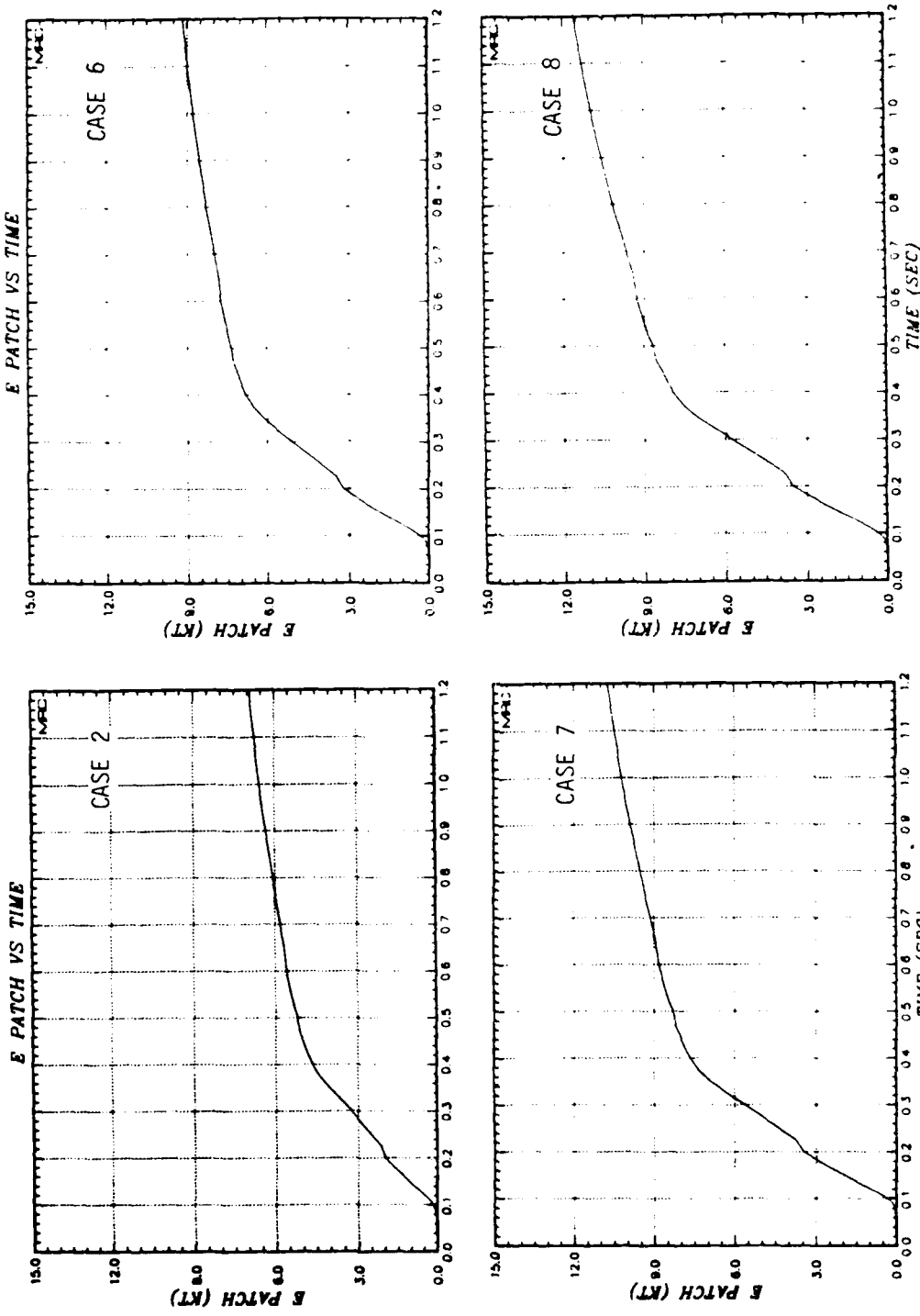

Figure 36. Patch energy as a function of time for CASE 2, CASE 6, CASE 7, and CASE 8.

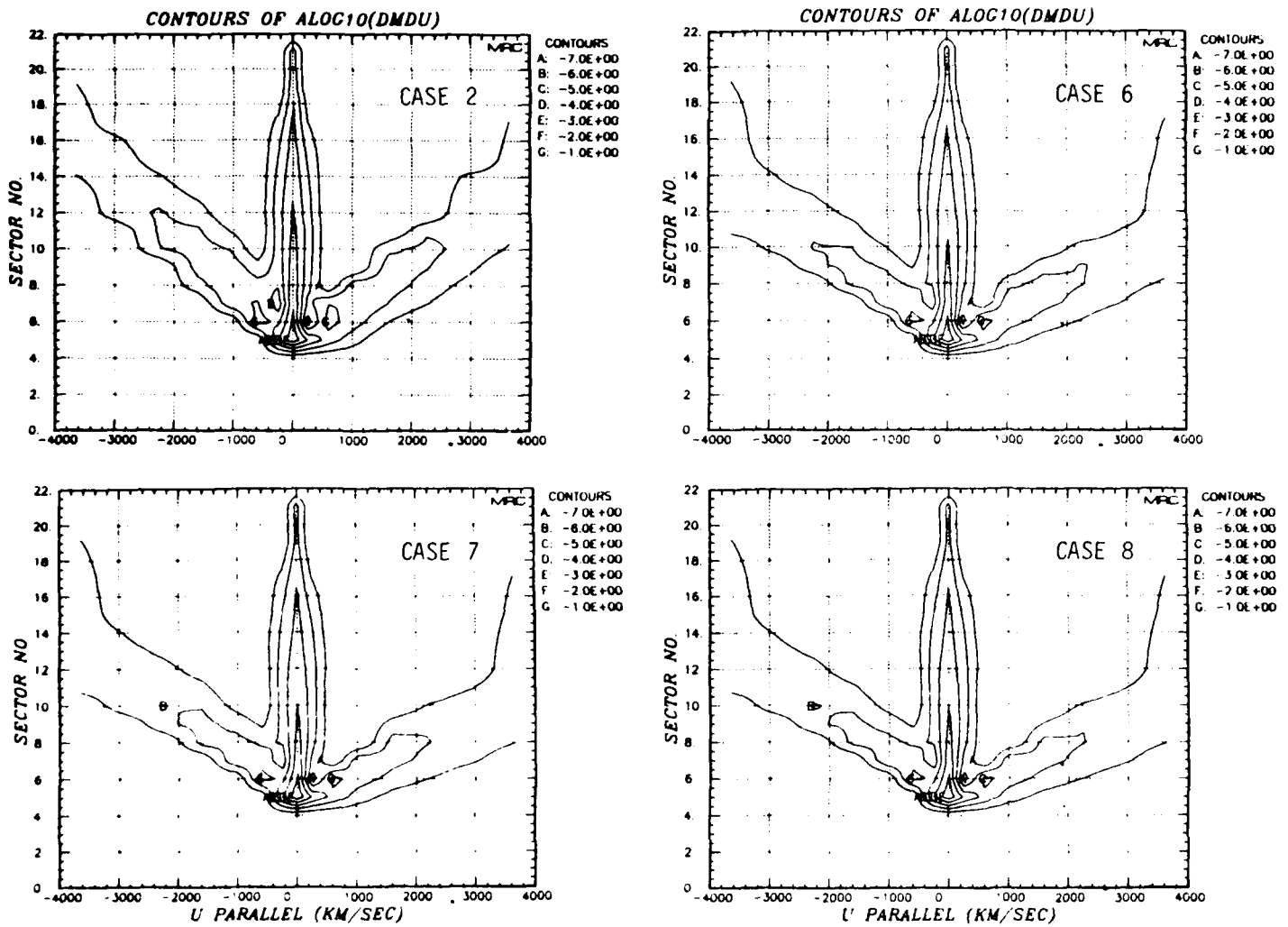

Figure 37. Comparison of distribution function contours for CASE 2, CASE 6, CASE 7, and CASE 8 at .05 seconds.

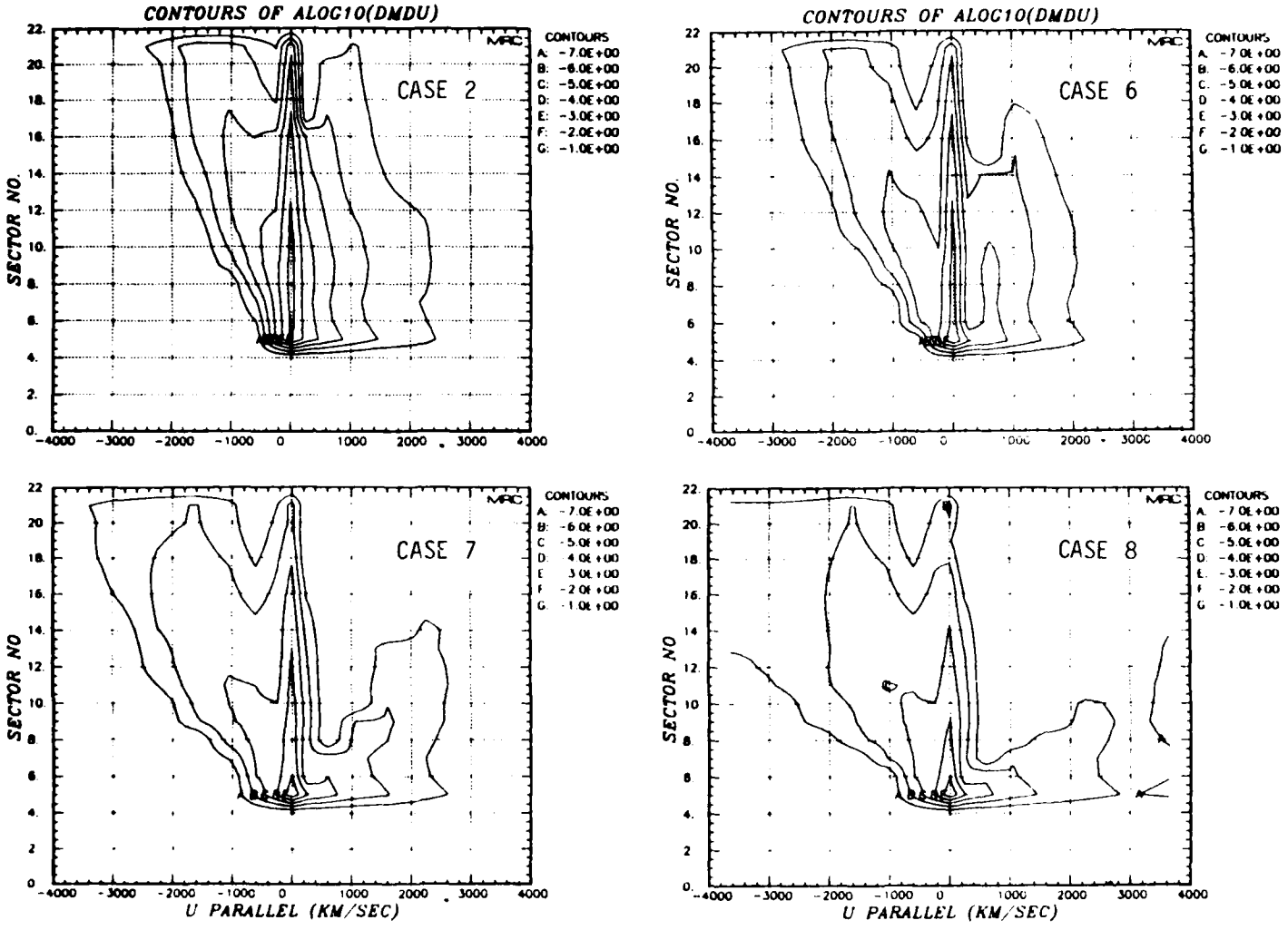

Figure 38. Comparison of distribution function contours for CASE 2, CASE 6, CASE 7, and CASE 8 at .40 seconds.

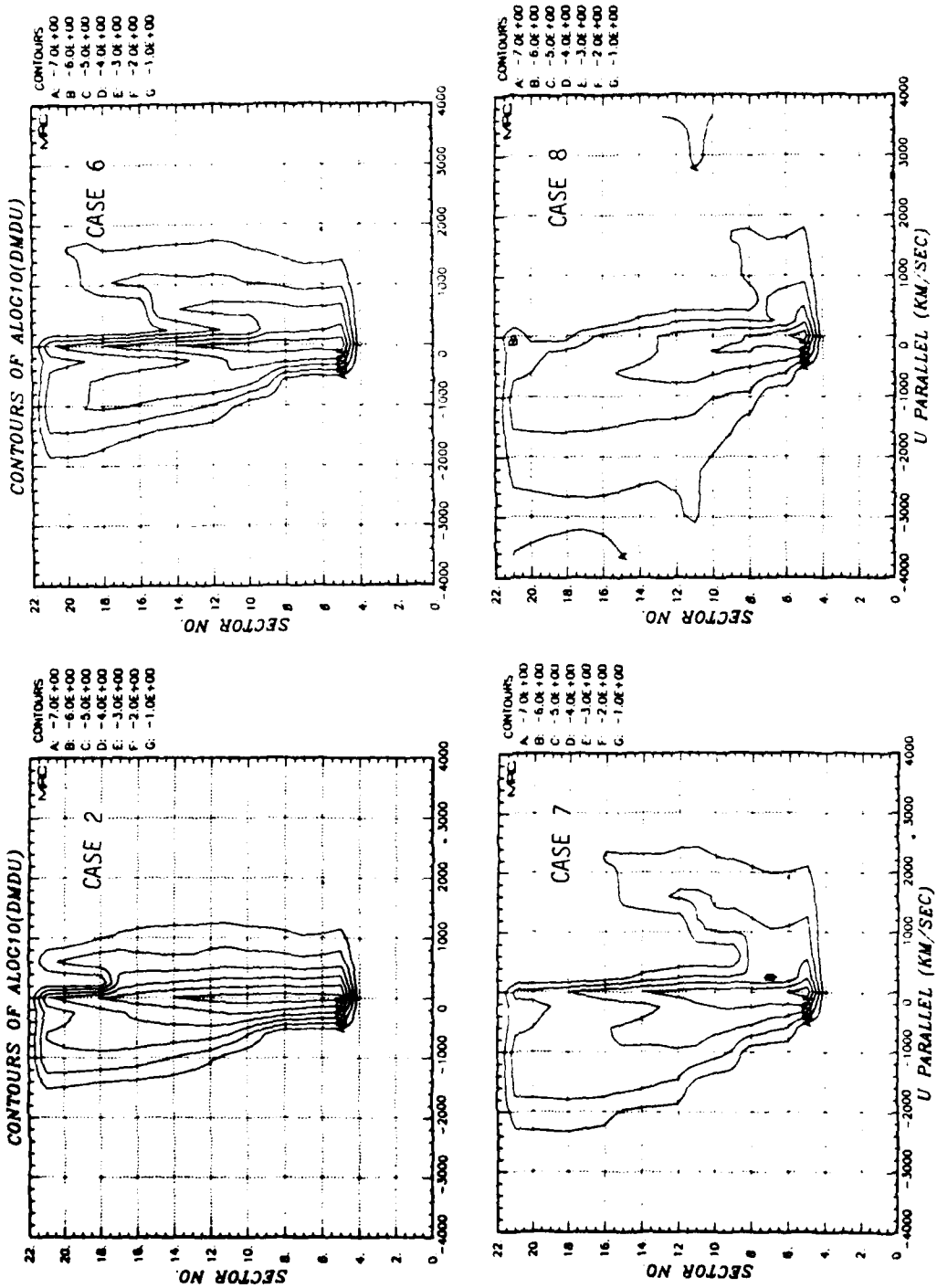

Figure 39. Comparison of distribution function contours for CASE 2, CASE 6, CASE 7, and CASE 8 at 1.00 seconds.

functions. At .05 seconds, the differences are relatively minor, but at .4 seconds and at 1 second, there are substantial differences. The most obvious differences are that the reduced mass cases show contours at larger velocities than does the nominal WP CASE 2. Not quite so obvious, although equally important, is the fact that as the added mass is reduced, the low velocity portion of the distribution is reduced. This is clearly evident in the comparison of patch spectra, given in Figure 40. The mass added to the flux tube through collisional ionization of background air has a dramatic effect on the character of the patch spectrum. Without this added ion mass, most of the energy arrives in the patch at large velocities, but with it, the patch spectrum peaks at low velocities.

Thus, we conclude from this parameter study that while the high velocity portion of the patch spectrum shows substantial dependence on the details of the plasma instability model, the low velocity portion is relatively insensitive to it. On the other hand, the entire spectrum is sensitive to the rate at which background air is ionized in the expanding blast wave and subsequently shares the available thermal energy. This is a fortunate result, because we have a great deal more confidence in our ability to treat collisional ionization properly than in our ability to accurately model plasma instabilities.

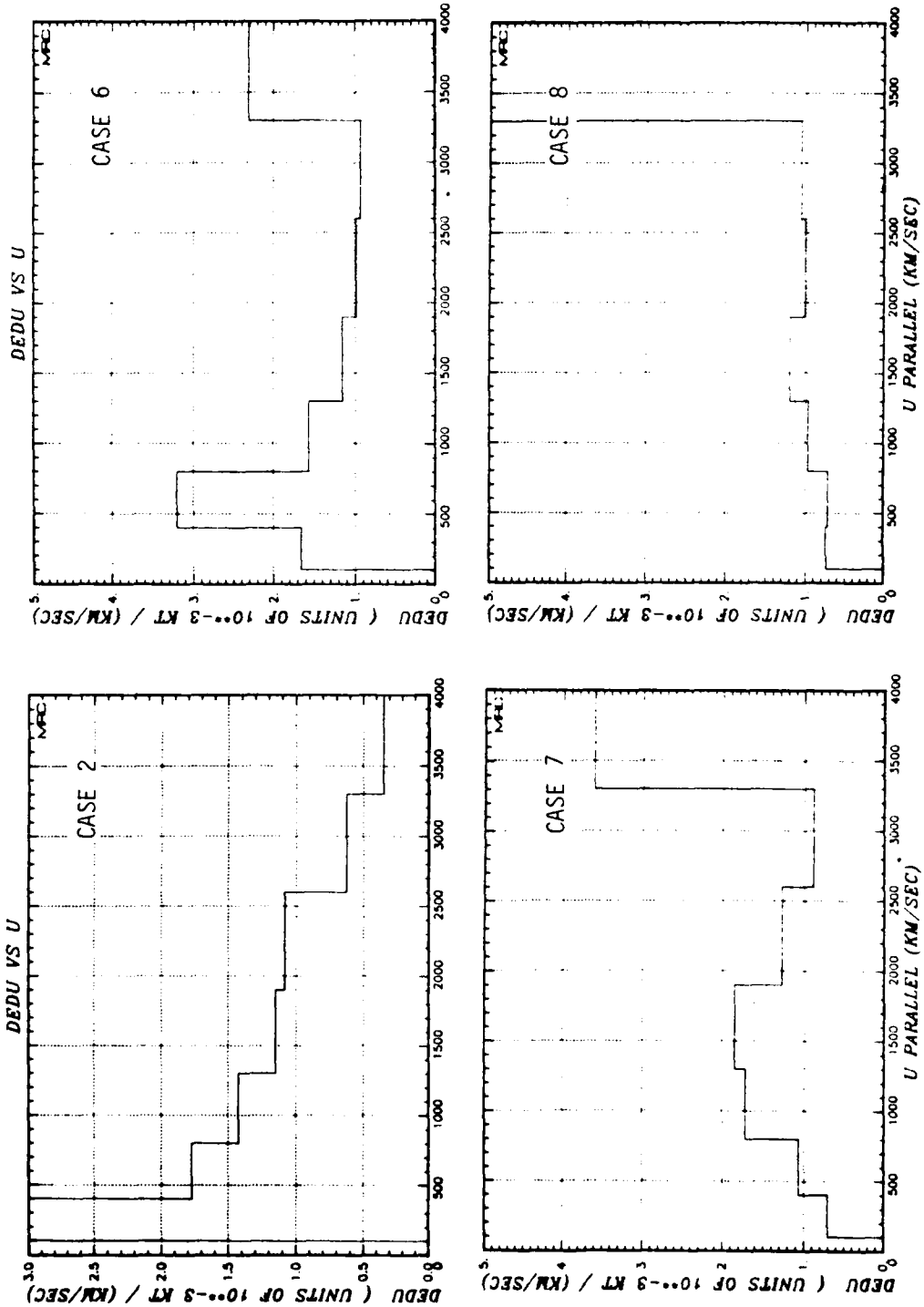

Figure 40. Comparison of patch spectra for CASE 2, CASE 6, CASE 7, and CASE 8.

REFERENCES

1. Longmire, C. L., et. al., 1962, private communication.
2. Longmire, C. L., R. W. Kilb, and W. F. Crevier, "The CMHD Approach to High Altitude Blast Waves," DNA 3313 T, Mission Research Corporation July 1974.
3. Kilb, R. W., and D. E. Glenn, June 1978, private communication.
4. Spitzer, Lyman, Jr., "Physics of Fully Ionied Gases" 2nd Edition, Interscience Publishers, 1962.
5. Schlueter, W. A., and J. K. Buckner, June 1970, private communication.
6. Hain, K. et. al., November 1980, private communication.

DISTRIBUTION LIST

DEPARTMENT OF DEFENSE

Assistant to the Secretary of Defense
Atomic Energy
ATTN: Executive Assistant

Command & Control Tech Ctr
ATTN: C-650

Defense Communications Agency
ATTN: J300 for Yen-Sun Fu
ATTN: Code 230
ATTN: Code 205

Defense Comm Engineer Ctr
ATTN: Code R410, N. Jones
ATTN: Code R410, R. Craighill
ATTN: Code R123
ATTN: Code R410

Defense Nuclear Agency
ATTN: STNA
ATTN: RAAE, W. McKechney
ATTN: RAAE, H. Fitz Jr
ATTN: RAAE, P. Lunn
3 cy ATTN: RAAE
4 cy ATTN: TITL

Defense Technical Information Center
12 cy ATTN: DD

Dep Under Secretary of Defense
Comm, Cmd, Cont & Intell
ATTN: Dir of Intelligence Sys

Field Command
DNA Det 1
Lawrence Livermore Lab
ATTN: FC-1

Field Command
Defense Nuclear Agency
ATTN: FCTT, G. Ganong
ATTN: FCPR
ATTN: FCTT, W. Summa
ATTN: FCTT
ATTN: FCTXE

Interservice Nuclear Weapons School
ATTN: TTV

Joint Chiefs of Staff
ATTN: C3S Evaluation Office (HDOO)

Joint Strat Tgt Planning Staff
ATTN: JLTW-2

National Security Agency
ATTN: R-52, J. Skillman

Under Secretary of Def for Rsch & Engrg
ATTN: Strat & Thtr Nuc Forces, B. Stephan
ATTN: Strat & Space Sys, OS
ATTN: Defensive Systems

WWMCCS Systems Engineering Org
ATTN: R. Crawford

DEPARTMENT OF THE ARMY

Atmospheric Sciences Laboratory
ATTN: DELAS-EO, F. Niles

BMD Advanced Technology Ctr
ATTN: ATC-R, W. Dickinson
ATTN: ATC-R, D. Russ
ATTN: ATC-O, W. Davies
ATTN: ATC-T, M. Capps

BMD Systems Command
ATTN: BMDSC-HLE, R. Webb
2 cy ATTN: BMDSC-HW

Dep Ch of Staff for Rsch Dev & Acq
ATTN: DAMA-CSS-N
ATTN: DAMA-CSZ-C
ATTN: DAMA-WSZ-C

Electronics Tech & Devices Lab
ATTN: DELET-R, S. Kronenberg

Harry Diamond Laboratories
2 cy ATTN: DELHD-NW-P

US Army Ballistic Research Labs
ATTN: DRDAR-TSB-S
ATTN: DRDAR-BLB, J. Mester

US Army Chemical School
ATTN: ATZN-CM-CS

US Army Comm-Elec Engrg Instal Agency
ATTN: CCC-EMEO-PED, G. Lane

US Army Foreign Science & Tech Ctr
ATTN: DRXST-SD

US Army Materiel Dev & Readiness Cmd
ATTN: DRCLDC, J. Bender

US Army Nuclear & Chem Agency
ATTN: Library

US Army Research Office
ATTN: R. Mace

US Army Satellite Comm Agency
ATTN: Document Control

US Army TRADOC Sys Analysis Actvy
ATTN: ATAA-PL

USA Missile Command
ATTN: DRSMI-YSO, J. Gamble

DEPARTMENT OF THE NAVY

Naval Electronic Systems Command
ATTN: PME 106-13, T. Griffin
ATTN: PME-117-2013, G. Burnhart
ATTN: PME 117-211, B. Kruger
ATTN: PME 106-4, S. Kearney
ATTN: PME 117-20
ATTN: Code 501A

DEPARTMENT OF THE NAVY (Continued)

Naval Intelligence Support Ctr
ATTN: Document Control
ATTN: NISC-50

Naval Ocean Systems Center
ATTN: Code 5322, M. Paulson
ATTN: Code 5323, J. Ferguson
ATTN: Code 532

Naval Postgraduate School
ATTN: Code 1424 Library

Naval Research Laboratory
ATTN: Code 4187
ATTN: Code 6780, J. Fedder
ATTN: Code 4139, D. McNutt
ATTN: Code 4780, S. Ossakow
ATTN: Code 4780, D. Strobel
ATTN: Code 4720, J. Davis
ATTN: Code 6700, T. Coffey
ATTN: Code 7500, B. Wald
ATTN: Code 4700.1, W. Ali
ATTN: Code 2627
ATTN: Code 2000, J. Brown
ATTN: Code 6700
ATTN: Code 4128.2, J. Hohnson
ATTN: Code 7950, J. Goodman

Naval Surface Weapons Center
ATTN: Code X211
ATTN: Code F31

Ofc of the Dep Ch of Naval Ops
ATTN: OP 941D

Strat Systems Project Office
ATTN: NSP-2722, F. Wimberly
ATTN: NSP-2141
ATTN: NSP-43, Tech Lib

DEPARTMENT OF THE AIR FORCE

Aeronautical Systems Division
ATTN: ASD/YH-YEF, Capt Guice

Air Force Geophysics Lab
ATTN: OPR-1
ATTN: OPR, H. Gardiner
ATTN: R. O'Neil
ATTN: PHP
ATTN: PHI, J. Buchau
ATTN: R. Babcock
2 cy ATTN: OPR, R. Murphy
2 cy ATTN: LKB, K. Champion
2 cy ATTN: LKD, R. Narcisi
2 cy ATTN: LKO, R. Huffman
2 cy ATTN: OPR, J. Kennealy
4 cy ATTN: CA, A. Stair

Air Force Office of Scientific Rsch
ATTN: AFOSR/NC

Air force Systems Command
ATTN: DLAE
ATTN: DLS
ATTN: DLTW
ATTN: DLXP
ATTN: SDR

DEPARTMENT OF THE AIR FORCE (Continued)

Air Force Tech Applications Ctr
ATTN: TN
ATTN: TF
ATTN: TD
ATTN: Tech Library

Air Force Weapons Lab
ATTN: NTYC
ATTN: SUL

Air Force Wright Aeronautical Lab
ATTN: A. Johnson
ATTN: W. Hunt

Air University Library
ATTN: AUL-LSE

Air Weather Service, MAC
ATTN: DNXP, R. Prochaska

Assistant Chief of Staff
Studies & Analyses
ATTN: AF/SASC, C. Rightmeyer

Ballistic Missile Office
ATTN: ENSN W. Wilson
ATTN: SYC, Col Kwan
ATTN: SYDT

Deputy Chief of Staff
Research, Development & Acq
3 cy ATTN: AFRDS, Space Sys & C3 Dir

Foreign Technology Division
ATTN: NIIS Library

Rome Air Development Cntr
ATTN: OCD, J. Simons
ATTN: TSLD

Space Division
ATTN: WE
ATTN: YGJB, W. Mercer
ATTN: YGP
ATTN: YKM, Capt Norton
ATTN: YN, P. Sivgals

Strategic Air Command
ATTN: ADWATE, B. Bauer
ATTN: XPFS
ATTN: NRT

DEPARTMENT OF ENERGY

Department of Energy
ATTN: OMA

OTHER GOVERNMENT AGENCIES

Central Intelligence Agency
ATTN: OSWR/SSD for K. Feuerpfeil
ATTN: OSWR/NED

Department of Commerce
National Bureau of Standards
ATTN: A. Phelps

OTHER GOVERNMENT AGENCIES (Continued)

Department of Commerce
National Bureau of Standards
ATTN: Sec Ofc for M. Krauss
ATTN: Sec Ofc for S. Abramowitz
ATTN: Sec Ofc for J. Devoe
ATTN: Sec Ofc for R. Levine

Department of Commerce
National Oceanic & Atmospheric Admin
3 cy ATTN: E. Ferguson
3 cy ATTN: F. Fehsenfeld

Institute for Telecomm Sciences
ATTN: G. Falcon
ATTN: W. Utlaut

NASA
ATTN: J. Watts
ATTN: W. Roberts
ATTN: W. Oran
ATTN: C. Balcher
ATTN: N. Stone

NASA
ATTN: Technical Library
ATTN: Code 6801, A. Tempkin
ATTN: Code 900, J. Siry
3 cy ATTN: A. Aiken

NASA
ATTN: P. Kurzhals
ATTN: J. Haughey
ATTN: A. Schardt
ATTN: ST-5, D. Cauffman

NASA
ATTN: MS-168, C. Schexnayder

NASA
ATTN: N-245-3, R. Whitten

NASA
ATTN: J. Gray

DEPARTMENT OF ENERGY CONTRACTORS

EG&G, Inc
ATTN: D. Wright
ATTN: J. Colvin

University of California
Lawrence Livermore National Lab
ATTN: L-48, E. Woodward
ATTN: L-325, G. Haugan
ATTN: L-10, H. Kruger
ATTN: L-71, J. Chang
ATTN: L-31, R. Hager
ATTN: L-389, R. Ott
ATTN: Technical Info Dept Library
ATTN: L-262, W. Duewer
ATTN: L-262, D. Wuebbles

Sandia National Lab
ATTN: Org 1250, W. Brown
ATTN: L. Anderson
ATTN: Org 4231, T. Wright
ATTN: M. Kramm
ATTN: Tech Lib 3141
ATTN: D. Dahlgren

DEPARTMENT OF ENERGY CONTRACTORS (Continued)

Sandia National Labs, Livermore
ATTN: T. Cook

Los Alamos National Lab
ATTN: Librarian
ATTN: MS362 Library
ATTN: T. Kunkle, ESS-5
ATTN: M. Sandford
ATTN: MS 670, J. Hopkins
ATTN: G. Davis
ATTN: MS 664, J. Zinn
ATTN: D. Simons
ATTN: R. Jeffries
ATTN: J. Wolcott
ATTN: G. Barrasch
ATTN: R. Carlos
ATTN: H. Argo
ATTN: M. Pongratz

DEPARTMENT OF DEFENSE CONTRACTORS

Aero-Chem Research Labs, Inc
ATTN: A. Fontijn

Aerodyne Research, Inc
ATTN: M. Camac
ATTN: J. Wormhoudt
ATTN: C. Kolb

Aerospace Corp
ATTN: V. Josephson
ATTN: R. Slaughter
ATTN: J. Straus
ATTN: H. Mayer
ATTN: T. Widhoph
ATTN: N. Cohen
ATTN: J. Reinheimer
ATTN: I. Garfunkel
ATTN: D. Olsen

AVCO Everett Research Lab, Inc
ATTN: A830
ATTN: C. Von Rosenberg Jr
ATTN: Tech Library

Battele Memorial Institute
ATTN: H. Lamuth
ATTN: STOIAC
ATTN: R. Thatcher

Berkeley Research Associates, Inc
ATTN: J. Workman
ATTN: S. Brecht
ATTN: C. Prettie

Boeing Aerospace Co
ATTN: MS/87-63, D. Clauson

Boston College
ATTN: W. Greider
ATTN: E. Hegblom

Boston College
2 cy ATTN: Chairman Dept of Chemistry
2 cy ATTN: Chairman Dept of Physics

University of California at Riverside
ATTN: A. Lloyd
ATTN: J. Pitts Jr

DEPARTMENT OF DEFENSE CONTRACTORS (Continued)

University of California at San Diego
ATTN: H. Booker

Calspan Corp
ATTN: W. Wurster
ATTN: M. Dunn
ATTN: J. Grace
ATTN: C. Treanor

Charles Stark Draper Lab, Inc
ATTN: J. Gilmore
ATTN: A. Tetewski
ATTN: D. Cox

University of Colorado
ATTN: G. Lawrence-LASP
ATTN: C. Lineberger-JILA

Columbia University
ATTN: Security Officer for H. Foley

Computer Sciences Corp
ATTN: F. Eisenbarth

Comsat Labs
ATTN: D. Fang

Concord Sciences
ATTN: E. Sutton

Cornell University
ATTN: M. Kelly
ATTN: D. Farley Jr

University of Denver
ATTN: Sec Officer for D. Murcray

University of Denver
ATTN: B. Van Zyl

E-Systems, Inc
ATTN: R. Berezdivin

Electrospace Systems, Inc
ATTN: P. Phillips

Environmental Rsch Inst of Michigan
ATTN: IRIA Library

ESL, Inc
ATTN: J. Marshall
ATTN: R. Heckman
ATTN: R. Ibaraki
ATTN: E. Tsui
ATTN: J. Lehman

General Electric Co
ATTN: R. Edsall
ATTN: P. Zavitsanos

General Electric Co
ATTN: F. Reibert

General Research Corp
ATTN: J. Ise Jr
ATTN: B. Bennett

Geo-Centers
ATTN: E. Marram

DEPARTMENT OF DEFENSE CONTRACTORS (Continued)

Harris Corp
ATTN: E. Knick

Horizons Technology, Inc
ATTN: R. Kruger

HSS, Inc
ATTN: D. Hansen

Institute for Defense Analyses
ATTN: H. Gates
ATTN: H. Wolfhard
ATTN: E. Bauer

International Tel & Telegraph Corp
ATTN: Technical Library

JAYCOR
ATTN: J. Sperling

Kaman Sciences Corp
ATTN: J. Jordano

Kaman Sciences Corp
ATTN: T. Stephens

Kaman Tempo
ATTN: W. Knapp
ATTN: B. Gambill
ATTN: J. Devore
ATTN: K. Schwartz
ATTN: W. McNamara
ATTN: J. Devore
ATTN: V. Stull
5 cy ATTN: DASIAC

Lockheed Missiles & Space Co, Inc
ATTN: D. Divis

Lockheed Missiles & Space Co, Inc
ATTN: J. Perez
ATTN: J. Cladis
ATTN: M. Walt
ATTN: J. Reagan
ATTN: J. Kumer
ATTN: B. McCormac
ATTN: R. Sears

Lockheed Missiles & Space Co, Inc
ATTN: C. Old
ATTN: D. Churchill

University of Lowell
ATTN: G. Best

MIT Lincoln Lab
ATTN: D. Towle

MA/COM Linkabit Inc
ATTN: I. Jacobs
ATTN: H. Van Trees
ATTN: A. Viterbi

Magnavox Govt & Indus Elec Co
ATTN: G. White

Martin Marietta Corp
ATTN: R. Heffner

DEPARTMENT OF DEFENSE CONTRACTORS (Continued)

McDonnell Douglas Corp
ATTN: Technical Library Services
ATTN: R. Halprin
ATTN: W. Olson

Meteor Communications Corp
ATTN: R. Leader

Mission Research Corp
ATTN: R. Bigoni
ATTN: R. Bogusch
ATTN: S. Gutsche
ATTN: P. Fischer
ATTN: F. Guigliano
ATTN: G. McCartor
ATTN: D. Archer
ATTN: M. Scheibe
ATTN: C. Lauer
ATTN: R. Hendrick
4 cy ATTN: R. Kilb
4 cy ATTN: F. Fajen
5 cy ATTN: Tech Library

Mitre Corp
ATTN: MS J104, M. Dresp
ATTN: B. Adams

Mitre Corp
ATTN: W. Hall
ATTN: J. Wheeler
ATTN: W. Foster

Pacific-Sierra Research Corp
ATTN: H. Brode, Chairman SAGE

Photometrics, Inc
ATTN: I. Kofsky

Physical Dynamics, Inc
ATTN: A. Thompson

Physical Dymanics, Inc
ATTN: E. Fremouw

Physical Research, Inc
ATTN: R. Deliberis

Physical Science Lab
ATTN: W. Berning

Physical Sciences, Inc
ATTN: G. Caledonia
ATTN: K. Wray
ATTN: R. Taylor

Physics International Co
ATTN: Technical Library

Univ of the Commonwealth, Pittsburgh
ATTN: F. Kaufman
ATTN: W. Fite
ATTN: M. Biondi

Princeton University
ATTN: Librarian

R&D Associates
ATTN: B. Yoon
ATTN: J. Rosengren

DEPARTMENT OF DEFENSE CONTRACTORS (Continued)

R&D Associates
ATTN: W. Karzas
ATTN: R. Turco
ATTN: R. Lelevier
ATTN: R. Lindgren
ATTN: H. Ory
ATTN: F. Gilmore
ATTN: M. Gantsweg
ATTN: B. Gabbard

Rand Corp
ATTN: E. Bedrozian
ATTN: C. Crain

Science Applications, Inc
ATTN: D. Hamlin
ATTN: D. Sachs
ATTN: L. Linson

Science Applications, Inc
ATTN: J. Cockayne

Space Data Corp
ATTN: S. Fisher

Spectral Sciences, Inc
ATTN: F. Bein

SRI International
ATTN: G. Smith
ATTN: R. Tsunoda
ATTN: J. Vickrey
ATTN: M. Baron
ATTN: C. Rino
ATTN: D. McDaniels
ATTN: W. Jaye
ATTN: V. Gonzales
ATTN: R. Hake Jr
ATTN: R. Leadabrand
ATTN: W. Chesnut
ATTN: J. Casper

SRI International
ATTN: C. Hulburt

Stewart Radiance Lab
ATTN: J. Ulwich

Sylvania Systems Group
ATTN: R. Steinhoff

Sylvania Systems Group
ATTN: J. Concordia
ATTN: I. Kohlberg

Technology International Corp
ATTN: W. Boquist

Teledyne Brown Engineering
ATTN: J. Ford
ATTN: MS-12 Tech Library
ATTN: F. Leopard
ATTN: N. Passino

TRW Electronics & Defense Sector
ATTN: R. Plebuch

Wayne State University
ATTN: R. Kummler

DEPARTMENT OF DEFENSE CONTRACTORS (Continued)

Utah State University
ATTN: Sec Con ofc for K. Baker
ATTN: Sec Con ofc for D. Baker
ATTN: Sec Con ofc for C. Wyatt
ATTN: Sec Con ofc for A. Steed
ATTN: Sec Con ofc for D. Burt

Wayne State University
ATTN: W. Kauppila

DEPARTMENT OF DEFENSE CONTRACTORS (Continued)

Visidyne, Inc
ATTN: W. Reidy
ATTN: T. Degges
ATTN: C. Humphrey
ATTN: O. Shepard
ATTN: J. Carpenter
ATTN: H. Smith

California Institute of Technology
ATTN: J. Ajello